

See discussions, stats, and author profiles for this publication at: <https://www.researchgate.net/publication/369592313>

GlassNet: a multitask deep neural network for predicting many glass properties

Preprint · March 2023

CITATIONS
0

READS
96

1 author:



Daniel R Cassar

Centro Nacional de Pesquisa em Energia e Materiais

51 PUBLICATIONS 691 CITATIONS

SEE PROFILE

Some of the authors of this publication are also working on these related projects:



Exploring the link between crystallization kinetics and cooperatively rearranging regions in supercooled liquids [View project](#)



Laser-heated Glass and Glass-ceramic preparation [View project](#)

GlassNet: a multitask deep neural network for predicting many glass properties

Daniel R. Cassar

Ilum School of Science, Brazilian Center for Research in Energy and Materials (CNPEM), Zip Code 13083-970, Campinas, São Paulo, Brazil.
daniel.cassar@ilum.cn pem.br

Abstract

A multitask deep neural network model was trained on more than 218k different glass compositions. This model, called GlassNet, can predict 85 different properties (such as optical, electrical, dielectric, mechanical, and thermal properties, as well as density, viscosity/relaxation, crystallization, surface tension, and liquidus temperature) of glasses and glass-forming liquids of different chemistries (such as oxides, chalcogenides, halides, and others). The model and the data used to train it are available in the `GlassPy` Python module as free and open source software for the community to use and build upon. As a proof of concept, GlassNet was used with the MYEGA viscosity equation to predict the temperature dependence of viscosity and outperformed another general purpose viscosity model available in the literature (ViscNet) on unseen data. An explainable AI algorithm (SHAP) was used to extract knowledge correlating the input (physicochemical information) and output (glass properties) of the model, providing valuable insights for glass manufacturing and design. It is hoped that GlassNet, with its free and open source nature, can be used to enable faster and better computer-aided design of new technological glasses.

Keywords: non-metallic glasses, artificial neural networks, property prediction

1 Introduction

Glasses are particularly interesting materials for data-driven modeling. First, there is no need for crystal structure descriptors, because these materials are noncrystalline. Second, commercial glass properties are highly dependent on glass chemical composition, because the vast majority of these glasses are manufactured by the same process, the melt and quench technique [1]. These facts are often exploited in the literature with good to great results [2]–[9].

Recently, Le Losq et al. [10] reported a new model called i-Melt, which is a multitask deep neural network capable of predicting 18 different properties of melts and glasses in the K_2O – Na_2O – Al_2O_3 – SiO_2 system. A multitask model is a single model that has more than one output [11]. The expectation is that learning how to predict one output can help in predicting another related output.

This work is inspired by i-Melt. The goal is to test whether multitask learning can be beneficial to glass modeling when we increase the scope of the model, both the input (more glass chemistries) and the output (more properties). In the literature, single-output neural

networks are viable algorithms for glass modeling [12]–[22]. However, multitask models have not been explored except for the work of Le Losq et al. [10].

The main hypothesis investigated in this work was H_1 : multitask learning improves the performance of predictive models of glass properties.

2 Materials and methods

2.1 Data acquisition and processing

The SciGlass database, which is openly available to the community as a GitHub repository [23], provides the data used in this paper. This database consists of several dataframes. For this work, all the data in the main dataframe were collected. The processing steps for the raw data were as follows:

1. Only glasses with a sum of the molar fractions of the compounds between 0.99 and 1.01 were taken into account. Sum of molar fractions that are too far away from unity are probably due to typing errors.
2. Glasses with non-zero amounts of any compound in {"Al₂O₃+Fe₂O₃", "MoO₃+WO₃", "CaO+MgO", "FeO+Fe₂O₃", "Li₂O+Na₂O+K₂O", "Na₂O+K₂O", "F₂O-1", "FemOn", "HF+H₂O", "R₂O", "R₂O₃", "R₂O₃", "RO", "RmOn"} were removed. These compounds cannot be converted to atomic mass (see next step).
3. The chemical features were converted from compound molar fraction to atomic molar fraction. The atomic fractions were then rebalanced so that their sum is 1 for all examples.
4. Only the elements between atomic numbers 1 and 83 (hydrogen and bismuth included) were considered, excluding promethium and the noble gases. Glasses containing non-zero amounts of excluded elements were removed. This strategy will become clear in the next section when discussing feature extraction.
5. A total of 85 target properties were considered. Glasses without values for at least one property were removed. These properties and related information will be presented later.
6. Some of the properties were processed by setting an acceptable minimum or maximum value. These limits are shown in the Supplementary Material.

After these steps, the processed dataset had 281,093 examples with 919,164 filled target cells. Many target cells are unfilled, as expected. This is not an issue for inducing a neural network model, because the unfilled cells do not contribute in the backpropagation step [24].

The next step was deduplication, the removal of duplicate entries to avoid data leakage [25]. For this step, the atomic fraction was first rounded to the third decimal place, and then glasses with the same composition were grouped together and collapsed into a single entry. The resulting target value was the median of the targets from the duplicate groups, ignoring the unfilled cells. If all cells for a given target were unfilled, then the final collapsed cell was also unfilled. The median was chosen instead of the mean, because it is robust to outliers in small datasets.

After deduplication, the final dataset had 218,533 examples of different glasses, with 795,298 filled target cells. Finally, the data were shuffled and 10% were randomly selected to be part of the holdout dataset. These data were not used for anything else, except at the very end to test the predictive ability of the selected models (simulating what happens when the model sees new data). Hereafter, any reference to the dataset refers to the 90% of the data that was *not* selected for the holdout dataset, unless otherwise stated.

2.2 Feature extraction, feature selection, and data scaling

Inspired by the works of Ward et al. [26], Hu et al. [27], and Nakamura et al. [28], [29], we extracted physicochemical features from the chemical information of the glasses, following a similar procedure reported in a previous communication [19]. This procedure involved three steps.

The first step was to collect the physicochemical properties of the elements considered in this work (see step 4 of data processing in the previous section). A total of 55 elemental properties were collected using the Python modules `mendeleev` [30] and `matminer` [31]. The only restriction at this stage was that the property had to be available for all elements studied (justifying why promethium and noble gases were not considered in the previous section). See Table 1 for 25 of those 55 properties that were selected. The Supplementary Material lists the physicochemical properties that were considered but not selected.

The second step was using the physicochemical properties to compute new features. Let us consider one glass as an example. Let $\mathbf{C} = [x_{\text{H}}, x_{\text{Li}}, \dots, x_{\text{Bi}}]$ be a vector of the atomic mole fractions of the chemical elements that make this glass. Let $\mathbf{S} = [s_{\text{H}}, s_{\text{Li}}, \dots, s_{\text{Bi}}]$ be a vector of a certain physicochemical property s (atomic radius, for example). Each vector element of \mathbf{C} and \mathbf{S} correspond to the atomic mole fraction or physicochemical property of a chemical element. Having these vectors, we can compute the weighted features with

$$w = f(\mathbf{C} \circ \mathbf{S}) \quad (1)$$

and the absolute features with

$$a = f([\mathbf{C}] \circ \mathbf{S}). \quad (2)$$

In the equations above, f is an aggregator function, and \circ is the Hadamard product, also known as the element-wise product. The aggregator functions considered in this work are $\{\text{sum}, \text{min}, \text{max}, \text{mean}, \text{std}\}$.

The third step was feature selection. After the previous step, the dataset had 627 features: 77 representing the atomic mole fraction of the chemical elements, 275 representing the weighted physicochemical features (55 physicochemical properties times 5 aggregator functions), and 275 representing the absolute physicochemical features. The first procedure was to remove features with extremely low variance, defined as those with standard deviation lower than 10^{-3} . The second procedure was to remove features with high multicollinearity using the Variance Inflation Factor (VIF) [32]. The steps were:

1. Compute the VIF for all remaining features;
2. If all values of VIF are below 5, then stop;
3. Otherwise, remove the feature with the highest VIF and return to step 1.

The rationale of feature extraction is to add more relevant information to the problem to be leveraged by the algorithm when inducing the predictive model. The benefit of feature selection is twofold: reduce the computation power to induce the model (more features require more computation) [33], and reduce multicollinearity, which improves convergence of the model.

Finally, the dataset was scaled using a min-max scaler. This is a linear transformation that converts all features and targets to values between zero and one. This strategy is often used when training neural networks to improve convergence and reduce the difference in magnitude between features and targets.

2.3 Designing and training a multitask neural network

An artificial neural network (NN) algorithm was used to induce the predictive models of this work. More specifically, it was a multitask feedforward neural network (also known as a multilayer perceptron, MLP). This is a well-known algorithm in the machine learning field, and the formalism can be found elsewhere [34]. All NN models in this work were trained with `pytorch` [35] using `lightning` [36].

Backpropagation to adjust the NN weights and biases was performed using the weighted Adam optimizer. This optimizer was chosen based on the results of a previous publication [19]. At the start of training, 10% of the training data was randomly selected and reserved as the validation dataset. These data were not used to change the parameters (weights and biases) of the NN, but instead were used for the early stopping routine. This routine reduces overfitting of the NN by stopping its training after a certain number of epochs without improvement in the validation loss transpire. This number of epochs without improvement is a tunable hyperparameter called *patience*. An epoch is when all the training data “passes” through the neural network (forward pass) and then through backpropagation, and can be considered as one cycle of the training process.

Some of the hyperparameters (HP) of the algorithm were not part of the HP tuning; the loss function is one of them. We used the multitask loss function of Liebel and Körner [37], which combines the single-task loss (mean squared error) for each predicted property into a single number. This multitask loss function includes a regularization term with individual weights for each target. These weights are learnable parameters and their purpose is to avoid giving too much weight to those properties with much more data than others (appropriate for the unbalanced database studied).

Other hyperparameters of the algorithm were tuned and a total of 1000 different HP sets were tested. Table 2 shows the search space. The search was performed with the `ray[tune]` Python module [38], using an Asynchronous Successive Halving Algorithm (ASHA) scheduler [39] with a grace period of 20 and a reduction factor of 4. Search space navigation was performed with suggestions from a Tree-structured Parzen Estimator algorithm [40]. Each layer of the NN was allowed to have its own activation function (that is, the activation function of the hidden layers could be different). The activation functions considered were hyperbolic tangent, sigmoid, ReLU, Leaky ReLU, Softplus, GELU, ELU, PReLU, SiLU, SELU, and Mish. The maximum number of epochs for HP tuning was set to 1000.

After this initial search, 10 HP sets were selected for the next step, which was a 10-fold cross-validation. These 10 HP sets were manually selected from the best scoring sets (using multitask loss as the score), taking care to select *sufficiently different* network architectures. The rationale is that the top positions of these experiments commonly consist of neural networks that are far too similar; therefore, manually selecting different architectures increases the diversity of architectures to be tested. After cross-validation, the selected HP set was the one with the lowest mean loss considering the 10 local test datasets. This selected architecture will be discussed in the results section, but the reader can already check its hyperparameters in the far right column of Table 2.

The NN obtained is a multilayer perceptron. However, the network that inspired this work (i-Melt) is a multi-headed feedforward NN. Fortunately, one can be easily converted from the other within the `pytorch` framework. This gives us the opportunity to test a secondary hypothesis of this work H_2 : for the induction of multitask predictive models of glass properties, multi-headed feedforward neural networks have a better performance than multilayer perceptrons.

To test H_2 , we used a trained NN with the selected HP set and converted it into a multi-headed NN. We did so by replacing the last layer (output layer) with 85 new layers of 10 neurons each (ReLU activation function) in parallel, one layer for each property. These new layers are

relatively small and highly specialized for the prediction of their respective property.

The performance of the models was tested against the holdout dataset to see how they predicted new data. To test H₁, we compared these metrics with another model. The algorithm used to induce this comparative model was a random forest trained using the `scikit-learn` Python module with the default set of hyperparameters. The models induced by this algorithm had great performance in previous publications [4], [8].

After observing a reasonable performance of the NNs (discussed in the Results section), we proceeded to train the final model using the chosen architecture and considering *all* the dataset (training *and* holdout). This final model was given the name GlassNet.

Finally, relevant information for the glass community was obtained by computing the SHapley Additive exPlanation (SHAP) values using the `shap` Python module [41]–[43]. This is an analysis that allows the trained model to be interpreted in search of patterns that can then be used by glass scientists and engineers when designing new glasses. Unfortunately, it was not possible to obtain the interaction SHAP values recently used by the community [9], because this calculation cannot be performed for neural network-based models.

2.4 Modeling the temperature-dependence of viscosity

Knowledge of the temperature-dependence of shear viscosity is essential for glass manufacturing, because it is used to adjust process variables such as melting, working, and annealing temperatures. Recent publications have already reported on data-driven models for predicting this property, ViscNet [19] and i-Melt [10] being two examples of free and openly available data-driven viscosity models.

Many of the properties investigated in this work are directly or indirectly related to shear viscosity. Furthermore, many of these viscosity-related properties were better predicted by the multitask NNs than by the baseline model (discussed in detail in the Results section). Here, we exploited this fact by using the trained models to generate (temperature, viscosity) data tuples, and then using these data points to perform a non-linear regression of the MYEGA equation (Eq. 3), which is a physical model of viscosity [44].

$$\log_{10}(\eta(T)) = \log_{10}(\eta_\infty) + \frac{T_{12,M}}{T} [12 - \log_{10}(\eta_\infty)] \exp \left(\left[\frac{m}{12 - \log_{10}(\eta_\infty)} - 1 \right] \left[\frac{T_{12,M}}{T} - 1 \right] \right) \quad (3)$$

In the previous equation, η is the equilibrium shear viscosity, η_∞ is the asymptotic viscosity ($\eta_\infty \equiv \lim_{T \rightarrow \infty} \eta(T)$), m is the liquid fragility index [45], and $T_{12,M}$ has the same definition as T_{12} ($\eta(T_{12}) \equiv 10^{12}$ Pa. s), but it is written with a different notation to indicate that it comes from a non-linear regression of the MYEGA equation. Using this approach, GlassNet can predict three additional properties.

Knowing that the prediction of material properties by machine learning models is much more susceptible to noise (compared with prediction from experimental data), using a robust non-linear regression of Eq. (3) is a good strategy to compensate for this disadvantage. In this work, we used a Cauchy loss for the least squares regression. The mathematical equation for this loss is $\rho(z) = \ln(1 + z)$, where z is the standard least squares loss.

To test the viscosity prediction capabilities of GlassNet, a set of 143,219 data points of composition, temperature, and measured viscosity were collected from the SciGlass database. Entries containing thorium or uranium were removed, because GlassNet cannot predict glasses with either of these elements. Entries with $\log_{10}(\eta)$ outside the [-5, 12] range, measured at temperatures above 3000 K, or measured at temperatures below the glass transition (predicted by GlassNet) were also removed, because these data are prone to higher measurement errors. Composition (in atomic fraction) was rounded to the third decimal place and temperature (in

Kelvin) was rounded to the second decimal place before duplicate entries were merged into one with the median value of $\log_{10}(\eta)$. Finally, entries with the same chemical composition as one of the glasses used to train GlassNet were removed, to make this experiment another test of GlassNet’s predictive power for unseen compositions.

3 Results and discussion

3.1 Data analysis and selected physicochemical features

Table 1 lists the symbols used in this work, their meaning, and their units. Table 3 shows the descriptive statistics (count, minimum, mean, and maximum) of the 85 targets of GlassNet. These numbers reflect the whole dataset after data processing, just before the holdout split.

Of the 85 properties, 26 had more than 10k instances when all data were considered. In this group we find the glass transition temperature, density at ambient temperature, refractive index, Abbe number, Young’s modulus, microhardness, linear coefficient of thermal expansion below T_g , crystallization peak, crystallization onset, and others.

In contrast, 21 out of 85 properties had less than 1k examples. This group includes maximum crystal growth velocity, density and surface tension at temperatures above ambient, heat capacity at constant pressure, and others.

This representation problem regarding the number of examples of different targets can be an issue if left unattended. For example, the NN may choose to ignore the properties with less representation in favor of those with more data, defeating the purpose of having a multitask model. This problem is minimized by using the multitask loss function of Liebel and Körner [37], as discussed in the Materials and Methods section.

Table 4 shows the descriptive statistics (count, mean, and standard deviation) and elemental mole fraction information (first quartile, median, third quartile, and maximum) for the chemical elements in the glasses used to train GlassNet. These values reflect the full dataset just before the holdout split, similar to the data shown in Table 3.

Considering all the data, 25 of the 72 elements were present in more than 10k examples. In this group, we find the most common chemical elements of inorganic glasses such as oxygen, silicon, boron, sodium, aluminum, calcium, potassium, and others. Similarly, 14 of the 72 elements were present in fewer than 1k examples. In this group we find dysprosium, hafnium, europium, terbium, and others.

Remarkably, some elements in Table 4 have a maximum elemental mole fraction of 1, in other words, these are monoatomic examples present in the dataset, and it is known that most of them are quite resistant to glass formation [1]. While the original authors’ rationale for including these particular examples in the SciGlass database is not clear, the information in these entries is typically related to liquidus temperature, which (by definition) is a property of crystalline materials and not glasses. Given the small number of these data points and the importance of the liquidus temperature for glass making [1], these data points were not excluded.

The induced models will inevitably be better at predicting the properties of glasses with chemistries that are more represented in the training dataset. The expectation is that the strategy of physicochemical feature extraction from the data (see methods) will reduce this problem.

Finally, Table 5 shows the 98 selected features out of the 627 considered. Of these 98 features, 64 are elemental mole fractions, 12 are weighted physicochemical features (see Eq. 1), and 22 are absolute physicochemical features (see Eq. 2). Some remarks on these selected features: the aggregator function “mean” is not present; out of a total of 77 elemental mole

fraction features, 13 were not selected (e.g., silicon and oxygen are in this group of 13); out of a total of 55 physicochemical properties considered, only 25 are part of the selected features.

3.2 Neural network

The last column of Table 2 shows the hyperparameters selected after HP tuning. This is a deep neural network with four hidden layers. Each hidden layer has a different activation function. All hidden layers have a dropout probability that decreases from the first to the second layer and then keeps increasing until the last layer. Batch normalization is only present in the first two hidden layers.

The root mean squared error (RMSE) metrics of the NN models trained with the selected set of hyperparameters are shown in Table 3, one metric for each property. The values are the prediction metrics for the holdout dataset (*not* used to train the model) and the standard deviation is that obtained in the 10-fold cross-validation experiment. The RMSE gives an estimate of the prediction error in the same units and magnitude as the target. The same table also shows the RMSE for the random forest models (baseline model, used for comparison). A t-test (95% confidence) was used to compare how the three models performed; these results are also reported in Table 3.

The multi-headed NN model outperforms the multilayer perceptron model for 13 properties, 12 of which are properties with more than 10k examples. There was only one property for which the multi-headed model had a worse prediction, and that was $D(1073\text{ K})$. This result supports H₂; a multi-headed NN improves performance for targets with a large number of examples, without losing generalization power for targets with fewer examples.

Comparing the NN models with the random forest models produced mixed results: for 37 properties, there was no statistical difference between the performance of the random forest models and the NN models. The multilayer perceptron outperformed the random forest in 27 properties and was outperformed by the random forest in 21 properties. The multi-headed NN produced slightly better results: it outperformed the random forest in 30 properties and was outperformed by the random forest in 18 properties.

The properties that the NN predicted better than the random forest were mostly targets with more than one measurement at different temperatures, such as density measured at 1273 and 1673 K. Most of these properties are targets related to viscosity. Properties predicted better by random forest than NN were mostly targets with more than 10k examples.

Overall, neither supporting nor rejecting hypothesis H₁ is possible. On the one hand, a multitask NN improves the prediction of glass properties for targets with measurements in different experimental conditions (e.g., different temperatures), compared to specialized random forest models. Such improved prediction occurs because the shared hidden layers of a multitask NN can exploit the connections between the targets better than specialized models that “know” only one target. On the other hand, the specialized random forest models perform better when more data is available.

A computational advantage of the multitask NN over the random forest model is that it requires less memory to store the trained parameters. The parameters of the NN can be stored in an uncompressed binary file of less than 4 MiB, while the compressed files of all the random forest models require more than 1 GiB of storage. Inference is also slower for random forest models.

One question that arises from these results is whether the performance of the multitask neural network can be improved by target selection. For example, if one of the properties where the NN underperformed the random forest were removed, would the prediction of the remaining targets improve? A conservative hypothesis is that no, it would not improve performance, because the removed data is probably relevant to the overall learning. However, testing this

hypothesis is not the focus of this communication.

3.3 Interpreting the trained model

Figure 1 shows the SHAP value violin plots of three properties: $C_p(1073\text{ K})$, $T_{\max(U)}$, and $\log_{10}(\rho(1073\text{ K}))$. These plots show the 10 most important features (those with the highest mean absolute SHAP) on the y -axis, with SHAP values on the x -axis. The base value (marked as a vertical gray line) is the mean value of the property (considering the entire dataset) and has a SHAP value of zero. The width of the violins represents the number of examples with the same SHAP value, while the color within the violins represents the value of the feature. See the Supplementary Material for the violin plots for the other properties.

As shown in Figure 1a, $C_p(1073\text{ K})$ increases with increasing amounts of sodium, boron, magnesium, or calcium. Sodium is the element with the greatest impact on this property. Increasing the standard deviation of the boiling point of the elements present in the glass also increases this property. One can decrease this property by increasing the standard deviation of the FCC lattice parameter, the maximum atomic radius, the standard deviation of the effective nuclear charge, and the sum of the number of filled f valence orbitals. The heat capacity is a property related to the fluctuations in the glasses [46].

Figure 1b shows that sodium and boron are the most important features for modeling $T_{\max(U)}$. The modeling of this rather complex property involves many physicochemical features. With the exception of the melting enthalpy, the other physicochemical features shown in Figure 1b are not often discussed in the crystal growth literature. The temperature of the maximum crystal growth velocity is related to the glass-forming ability [47], and is one of key properties for glass-ceramics design, together with the glass transition temperature and the maximum crystal growth velocity [48].

Finally, Figure 1c shows sodium once again as the most important feature, this time for $\log_{10}(\rho(1073\text{ K}))$. Notably, 8 of the 10 most important features are elemental features for this property, the opposite of what was observed for $C_p(1073\text{ K})$ and $T_{\max(U)}$. This list includes elements that are well known in the electrical property community, like potassium, lithium, and vanadium.

The SHAP analysis allows us to answer other questions: What are the most relevant features overall (considering all the properties studied here)? And what are the most relevant features for each group of properties? Examining the frequency of the 10 most important features for each property is one strategy for answering these questions.

Table 6 shows the most frequent features overall and for property groups. Overall, we can see that some of the chemical elements that are most commonly used in glass making are also the most important ones in our analysis. Sodium, boron, lead, lithium, aluminum, potassium, and calcium are on this list. One might think that this is just a list of the most abundant chemical elements in the dataset, but this is not the case, as barium, magnesium, phosphorus, zinc, titanium, and fluor are not on this list (and they are all more abundant than lead in the dataset). Melting enthalpy, number of unfilled valence orbitals, and number of filled d orbitals are physicochemical features that are also collectively relevant to glass properties.

The most relevant features for viscosity and relaxation, optical properties, electrical and dielectric properties, mechanical properties, density, thermal properties, crystallization, and surface tension are also listed in Table 6. Again, sodium and boron are relevant features for most of these property groups. Lithium and lead are also relevant features, appearing many times in this table. Interestingly, the model understood that the optical properties are highly dependent on the filled valence orbitals (where the absorption process takes place) and on lead, bismuth, titanium, niobium, lanthanum, and germanium, known elements used for optical glasses.

These violin plots and the table of relevant features provide valuable insights for glass manufacturers and designers to help them fine-tune the properties of their products.

3.4 Viscosity modeling

The final viscosity dataset (after all the procedures mentioned in the Materials and Methods section) consisted of 134,976 examples. For each of these examples, the viscosity at the measurement temperature was predicted using GlassNet. To evaluate this prediction, the RMSE between the reported and predicted values of $\log_{10}(\eta)$ was calculated (with η in units of Pa.s). Glassnet had a RMSE of 0.65, performing better than ViscNet [19], another deep learning model used to predict viscosity, which had an RMSE of 1.1 for unseen data. However, GlassNet performed worse than i-Melt (RMSE: 0.4) [10] and the unnamed model reported by Tandia et al. (RMSE: 0.04) [3], two highly specialized models, trained and tested on liquids with much more restricted chemistries than GlassNet. The increase in RMSE can be considered the price paid for increasing the scope of GlassNet.

3.5 Model and data availability

The model reported here is called GlassNet and is available to the community, along with the training data, in the `GlassPy` Python module, a free and open source module for researchers working with glass materials. See the official repository at <https://github.com/drcassar/glasspy> for instructions on installing and using this module. In `GlassPy`, the user has the option to load the MLP or the multi-headed version of GlassNet. `GlassPy` can also use the random forest models, for those properties where random forest models outperformed the NNs (although, when doing this, the inference is slower). GlassNet can also predict the temperature-dependence of viscosity and the MYEGA parameters, as discussed in this paper.

`GlassPy` also provides an easy way to load SciGlass data into a `pandas` DataFrame, including (but not limited to) the GlassNet training dataset. These `pandas` DataFrames are state of the art Python objects for data analysis. Two advantages of using `GlassPy` as a frontend for exploring SciGlass data are

1. `GlassPy` already translates the SciGlass data into a ready-to-use DataFrame with an intuitive naming scheme;
2. `GlassPy` does not require installing any legacy non-free software (the official SciGlass repository only provides the database files in a legacy proprietary Microsoft Access format).

4 Summary and conclusion

In this work, we collected more than 218k different glass compositions with more than 795k data points on 85 properties. A new multitask neural network was designed and trained with this rich dataset. We observed that the trained multitask model outperformed specialized models (i.e., random forests) in predicting targets of the same property measured under different conditions (e.g., different temperatures). However, specialized models outperformed the multitask NN for some properties with many data points (more than 10k).

An advantage of the proposed model, compared to other models reported in the literature, is that it is not limited to a specific inorganic glass chemistry and can be used to predict properties of oxides, chalcogenides, halides, and other types of glasses.

We show how the purely data-driven predictions of the proposed model can be used together with a physical model to predict the temperature dependence of viscosity. This approach was

tested with about 135k viscosity data points and yielded better results than another general viscosity model (ViscNet [19]), but worse results than models designed for specific chemistries. Additionally, useful insights for glass manufacturing and design were obtained from the trained model using SHAP analysis.

The obtained model was named GlassNet and is free software, available to the community (together with the training data) in the Python module `GlassPy`. This free and open source suite for inorganic glass data and property prediction is expected to benefit the community, improve the reproducibility of data-driven publications, and accelerate the development of new and exciting glasses and glass-ceramics (e.g., by using GlassNet with inverse design tools such as GLAS [20]). In addition, the open nature of GlassNet allows the community to build on it to solve other property prediction problems using transfer learning [34], [49], [50].

Acknowledgements

The author acknowledges funding from the CNPq / INCT - Materials Informatics project. The author also thanks Carolina B. Zanelli for the English revision.

Declaration of Generative AI and AI-assisted technologies in the writing process

During the preparation of this work the author used Grammarly and DeepL in order to improve readability and grammar. After using these tools, the author reviewed and edited the content as needed and takes full responsibility for the content of the publication.

References

- [1] A. K. Varshneya and J. C. Mauro, *Fundamentals of Inorganic Glasses*, 3 edition. Elsevier, 2019.
- [2] S. Bishnoi *et al.*, “Predicting Young’s modulus of oxide glasses with sparse datasets using machine learning,” *Journal of non-crystalline solids*, vol. 524, p. 119643, 2019, doi: [10.1016/j.jnoncrysol.2019.119643](https://doi.org/10.1016/j.jnoncrysol.2019.119643).
- [3] A. Tandia, M. C. Onbasli, and J. C. Mauro, “Machine learning for glass modeling,” in *Springer Handbook of Glass*, J. D. Musgraves, J. Hu, and L. Calvez, Eds. Cham: Springer International Publishing, 2019, pp. 1157–1192.
- [4] E. Alcobaça *et al.*, “Explainable machine learning algorithms for predicting glass transition temperatures,” *Acta materialia*, vol. 188, pp. 92–100, 2020, doi: [10.1016/j.actamat.2020.01.047](https://doi.org/10.1016/j.actamat.2020.01.047).
- [5] B. Deng, “Machine learning on density and elastic property of oxide glasses driven by large dataset,” *Journal of non-crystalline solids*, vol. 529, p. 119768, 2020, doi: [10.1016/j.jnoncrysol.2019.119768](https://doi.org/10.1016/j.jnoncrysol.2019.119768).
- [6] Y. Tokuda, M. Fujisawa, D. M. Packwood, M. Kambayashi, and Y. Ueda, “Data-driven design of glasses with desirable optical properties using statistical regression,” *Aip advances*, vol. 10, no. 10, p. 105110, 2020, doi: [10.1063/5.0022451](https://doi.org/10.1063/5.0022451).
- [7] S. Bishnoi, R. Ravinder, H. S. Grover, H. Kodamana, and N. M. A. Krishnan, “Scalable Gaussian processes for predicting the optical, physical, thermal, and mechanical properties of inorganic glasses with large datasets,” *Materials advances*, vol. 2, no. 1, pp. 477–487, 2021, doi: [10.1039/DOMA00764A](https://doi.org/10.1039/DOMA00764A).
- [8] D. R. Cassar, S. M. Mastelini, T. Botari, E. Alcobaça, A. C. P. L. F. de Carvalho, and E. D. Zanotto, “Predicting and interpreting oxide glass properties by machine learning using

- large datasets,” *Ceramics international*, vol. 47, no. 17, pp. 23958–23972, 2021, doi: [10.1016/j.ceramint.2021.05.105](https://doi.org/10.1016/j.ceramint.2021.05.105).
- [9] R. Bhattoo, S. Bishnoi, M. Zaki, and N. M. A. Krishnan, “Understanding the compositional control on electrical, mechanical, optical, and physical properties of inorganic glasses with interpretable machine learning,” *Acta materialia*, vol. 242, p. 118439, 2023, doi: [10.1016/j.actamat.2022.118439](https://doi.org/10.1016/j.actamat.2022.118439).
- [10] C. Le Losq, A. P. Valentine, B. O. Mysen, and D. R. Neuville, “Structure and properties of alkali aluminosilicate glasses and melts: Insights from deep learning,” *Geochimica et cosmochimica acta*, vol. 314, pp. 27–54, 2021, doi: [10.1016/j.gca.2021.08.023](https://doi.org/10.1016/j.gca.2021.08.023).
- [11] R. Caruana, “Multitask Learning,” *Machine learning*, vol. 28, no. 1, pp. 41–75, 1997, doi: [10.1023/A:1007379606734](https://doi.org/10.1023/A:1007379606734).
- [12] C. Dreyfus and G. Dreyfus, “A machine learning approach to the estimation of the liquidus temperature of glass-forming oxide blends,” *Journal of non-crystalline solids*, vol. 318, no. 1-2, pp. 63–78, 2003, doi: [10.1016/S0022-3093\(02\)01859-8](https://doi.org/10.1016/S0022-3093(02)01859-8).
- [13] D. R. Cassar, A. C. P. L. F. de Carvalho, and E. D. Zanotto, “Predicting glass transition temperatures using neural networks,” *Acta materialia*, vol. 159, pp. 249–256, 2018, doi: [10.1016/j.actamat.2018.08.022](https://doi.org/10.1016/j.actamat.2018.08.022).
- [14] K. Yang *et al.*, “Predicting the Young’s Modulus of Silicate Glasses using High-Throughput Molecular Dynamics Simulations and Machine Learning,” *Scientific reports*, vol. 9, no. 1, p. 8739, 2019, doi: [10.1038/s41598-019-45344-3](https://doi.org/10.1038/s41598-019-45344-3).
- [15] T. Han, N. Stone-Weiss, J. Huang, A. Goel, and A. Kumar, “Machine learning as a tool to design glasses with controlled dissolution for healthcare applications,” *Acta biomaterialia*, vol. 107, pp. 286–298, 2020, doi: [10.1016/j.actbio.2020.02.037](https://doi.org/10.1016/j.actbio.2020.02.037).
- [16] J. N. P. Lillington, T. L. Goût, M. T. Harrison, and I. Farnan, “Predicting radioactive waste glass dissolution with machine learning,” *Journal of non-crystalline solids*, vol. 533, p. 119852, 2020, doi: [10.1016/j.jnoncrysol.2019.119852](https://doi.org/10.1016/j.jnoncrysol.2019.119852).
- [17] R. Ravinder *et al.*, “Deep learning aided rational design of oxide glasses,” *Materials horizons*, vol. 7, no. 7, pp. 1819–1827, 2020, doi: [10.1039/DOMH00162G](https://doi.org/10.1039/DOMH00162G).
- [18] S. K. Ahmmad, N. Jabeen, S. T. Uddin Ahmed, S. A. Ahmed, and S. Rahman, “Artificial intelligence density model for oxide glasses,” *Ceramics international*, vol. 47, no. 6, pp. 7946–7956, 2021, doi: [10.1016/j.ceramint.2020.11.144](https://doi.org/10.1016/j.ceramint.2020.11.144).
- [19] D. R. Cassar, “ViscNet: Neural network for predicting the fragility index and the temperature-dependency of viscosity,” *Acta materialia*, vol. 206, p. 116602, 2021, doi: [10.1016/j.actamat.2020.116602](https://doi.org/10.1016/j.actamat.2020.116602).
- [20] D. R. Cassar, G. G. Santos, and E. D. Zanotto, “Designing optical glasses by machine learning coupled with a genetic algorithm,” *Ceramics international*, vol. 47, no. 8, pp. 10555–10564, 2021, doi: [10.1016/j.ceramint.2020.12.167](https://doi.org/10.1016/j.ceramint.2020.12.167).
- [21] Y. Tokuda, M. Fujisawa, J. Ogawa, and Y. Ueda, “A machine learning approach to the prediction of the dispersion property of oxide glass,” *Aip advances*, vol. 11, no. 12, p. 125127, 2021, doi: [10.1063/5.0075425](https://doi.org/10.1063/5.0075425).
- [22] M. Zaki *et al.*, “Interpreting the optical properties of oxide glasses with machine learning and Shapely additive explanations,” *Journal of the american ceramic society*, vol. 105, no. 6, pp. 4046–4057, 2022, doi: [10.1111/jace.18345](https://doi.org/10.1111/jace.18345).
- [23] “Epam/SciGlass.” EPAM Systems, 2019. Accessed: Nov. 06, 2019. [Online]. Available: <https://github.com/epam/SciGlass>
- [24] D. E. Rumelhart, G. E. Hinton, and R. J. Williams, “Learning representations by back-propagating errors,” *Nature*, vol. 323, no. 6088, pp. 533–536, 1986, doi: [10.1038/323533a0](https://doi.org/10.1038/323533a0).
- [25] S. Kaufman, S. Rosset, C. Perlich, and O. Stitelman, “Leakage in data mining: Formulation, detection, and avoidance,” *Acm transactions on knowledge discovery from data*, vol. 6, no.

- 4, pp. 15:1–15:21, 2012, doi: [10.1145/2382577.2382579](https://doi.org/10.1145/2382577.2382579).
- [26] L. Ward, A. Agrawal, A. Choudhary, and C. Wolverton, “A general-purpose machine learning framework for predicting properties of inorganic materials,” *Npj computational materials*, vol. 2, no. 1, pp. 1–7, 2016, doi: [10.1038/npjcompumats.2016.28](https://doi.org/10.1038/npjcompumats.2016.28).
- [27] Y.-J. Hu *et al.*, “Predicting densities and elastic moduli of SiO₂-based glasses by machine learning,” *Npj computational materials*, vol. 6, no. 1, p. 25, 2020, doi: [10.1038/s41524-020-0291-z](https://doi.org/10.1038/s41524-020-0291-z).
- [28] K. Nakamura, N. Otani, and T. Koike, “Multi-objective Bayesian optimization of optical glass compositions,” *Ceramics international*, 2021, doi: [10.1016/j.ceramint.2021.02.155](https://doi.org/10.1016/j.ceramint.2021.02.155).
- [29] K. Nakamura, N. Otani, and T. Koike, “Search for oxide glass compositions using Bayesian optimization with elemental-property-based descriptors,” *Journal of the ceramic society of japan*, vol. 128, no. 8, pp. 569–572, 2020, doi: [10.2109/jcersj2.20118](https://doi.org/10.2109/jcersj2.20118).
- [30] L. Mentel, “mendeleev A Python resource for properties of chemical elements, ions and isotopes.” 2014. Available: <https://github.com/lmentel/mendeleev>
- [31] L. Ward *et al.*, “Matminer: An open source toolkit for materials data mining,” *Computational materials science*, vol. 152, pp. 60–69, 2018, doi: [10.1016/j.commatsci.2018.05.018](https://doi.org/10.1016/j.commatsci.2018.05.018).
- [32] D. W. Marquardt, “Generalized Inverses, Ridge Regression, Biased Linear Estimation, and Nonlinear Estimation,” *Technometrics*, vol. 12, no. 3, pp. 591–612, 1970, doi: [10.1080/00401706.1970.10488699](https://doi.org/10.1080/00401706.1970.10488699).
- [33] H. Liu, “Feature Selection,” in *Encyclopedia of Machine Learning*, C. Sammut and G. I. Webb, Eds. Boston, MA: Springer US, 2010, pp. 402–406. doi: [10.1007/978-0-387-30164-8_306](https://doi.org/10.1007/978-0-387-30164-8_306).
- [34] I. Goodfellow, Y. Bengio, A. Courville, and Y. Bengio, *Deep learning*, vol. 1. MIT press Cambridge, 2016. Available: <https://www.deeplearningbook.org/>
- [35] A. Paszke *et al.*, “PyTorch: An imperative style, high-performance deep learning library,” in *Advances in neural information processing systems 32*, H. Wallach, H. Larochelle, A. Beygelzimer, F. dAlché-Buc, E. Fox, and R. Garnett, Eds. Curran Associates, Inc., 2019, pp. 8024–8035. Available: <http://papers.neurips.cc/paper/9015-pytorch-an-imperative-style-high-performance-deep-learning-library.pdf>
- [36] W. Falcon and T. P. L. team, “PyTorch Lightning.” Zenodo, 2023. doi: [10.5281/zenodo.7688620](https://doi.org/10.5281/zenodo.7688620).
- [37] L. Liebel and M. Körner, “Auxiliary Tasks in Multi-task Learning.” arXiv, 2018. doi: [10.48550/arXiv.1805.06334](https://doi.org/10.48550/arXiv.1805.06334).
- [38] P. Moritz *et al.*, “Ray: A Distributed Framework for Emerging AI Applications.” arXiv, 2018. doi: [10.48550/arXiv.1712.05889](https://doi.org/10.48550/arXiv.1712.05889).
- [39] L. Li *et al.*, “A system for massively parallel hyperparameter tuning,” *Proceedings of machine learning and systems*, vol. 2, pp. 230–246, 2020.
- [40] J. Bergstra, D. Yamins, and D. Cox, “Making a science of model search: Hyperparameter optimization in hundreds of dimensions for vision architectures,” in *International Conference on Machine Learning*, 2013, pp. 115–123.
- [41] S. M. Lundberg and S.-I. Lee, “A unified approach to interpreting model predictions,” *Advances in neural information processing systems*, vol. 30, pp. 4765–4774, 2017, Accessed: Feb. 10, 2021. [Online]. Available: <https://proceedings.neurips.cc/paper/2017/hash/8a20a8621978632d76c43dfd28b67767-Abstract.html>
- [42] S. M. Lundberg *et al.*, “From local explanations to global understanding with explainable AI for trees,” *Nature machine intelligence*, vol. 2, no. 1, pp. 56–67, 2020, doi: [10.1038/s42256-019-0138-9](https://doi.org/10.1038/s42256-019-0138-9).
- [43] S. M. Lundberg *et al.*, “Explainable machine-learning predictions for the prevention of hypoxaemia during surgery,” *Nature biomedical engineering*, vol. 2, no. 10, pp. 749–760,

2018, doi: [10.1038/s41551-018-0304-0](https://doi.org/10.1038/s41551-018-0304-0).

- [44] J. C. Mauro, Y. Yue, A. J. Ellison, P. K. Gupta, and D. C. Allan, "Viscosity of glass-forming liquids," *Proceedings of the national academy of sciences of the united states of america*, vol. 106, no. 47, pp. 19780–19784, 2009, doi: [10.1073/pnas.0911705106](https://doi.org/10.1073/pnas.0911705106).
- [45] C. A. Angell, "Strong and fragile liquids," in *Relaxation in complex systems*, K. L. Ngai and G. B. Wright, Eds. Springfield: Naval Research Laboratory, 1985, pp. 3–12.
- [46] K. A. Kirchner *et al.*, "Beyond the Average: Spatial and Temporal Fluctuations in Oxide Glass-Forming Systems," *Chemical reviews*, vol. 123, no. 4, pp. 1774–1840, 2023, doi: [10.1021/acs.chemrev.1c00974](https://doi.org/10.1021/acs.chemrev.1c00974).
- [47] J. Jiusti, E. D. Zanotto, D. R. Cassar, and M. R. B. Andreetta, "Viscosity and liquidus-based predictor of glass-forming ability of oxide glasses," *Journal of the american ceramic society*, vol. 103, no. 2, pp. 921–932, 2020, doi: [10.1111/jace.16732](https://doi.org/10.1111/jace.16732).
- [48] E. D. Zanotto, "A bright future for glass-ceramics," *American ceramic society bulletin*, vol. 89, no. 8, pp. 19–27, 2010.
- [49] S. Bozinovski and A. Fulgosi, "The influence of pattern similarity and transfer learning upon training of a base perceptron b2," in *Proceedings of Symposium Informatica*, 1976, vol. 3, pp. 121–126.
- [50] S. Bozinovski, "Reminder of the First Paper on Transfer Learning in Neural Networks, 1976," *Informatica*, vol. 44, no. 3, 2020, doi: [10.31449/inf.v44i3.2828](https://doi.org/10.31449/inf.v44i3.2828).
- [51] A. K. Rappe, C. J. Casewit, K. S. Colwell, W. A. Goddard, and W. M. Skiff, "UFF, a full periodic table force field for molecular mechanics and molecular dynamics simulations," *Journal of the american chemical society*, vol. 114, no. 25, pp. 10024–10035, 1992, doi: [10.1021/ja00051a040](https://doi.org/10.1021/ja00051a040).
- [52] M. Rahm, R. Hoffmann, and N. W. Ashcroft, "Atomic and Ionic Radii of Elements 1–96," *Chemistry a european journal*, vol. 22, no. 41, pp. 14625–14632, 2016, doi: [10.1002/chem.201602949](https://doi.org/10.1002/chem.201602949).
- [53] W. M. Haynes, *CRC Handbook of Chemistry and Physics*. CRC Press, 2014.
- [54] T. Andersen, "Atomic negative ions: Structure, dynamics and collisions," *Physics reports*, vol. 394, no. 4, pp. 157–313, 2004, doi: [10.1016/j.physrep.2004.01.001](https://doi.org/10.1016/j.physrep.2004.01.001).
- [55] R. T. Sanderson, "An Explanation of Chemical Variations within Periodic Major Groups," *Journal of the american chemical society*, vol. 74, no. 19, pp. 4792–4794, 1952, doi: [10.1021/ja01139a020](https://doi.org/10.1021/ja01139a020).
- [56] R. T. Sanderson, "An Interpretation of Bond Lengths and a Classification of Bonds," *Science*, vol. 114, no. 2973, pp. 670–672, 1951, doi: [10.1126/science.114.2973.670](https://doi.org/10.1126/science.114.2973.670).
- [57] C. Tantardini and A. R. Oganov, "Thermochemical electronegativities of the elements," *Nature communications*, vol. 12, no. 1, p. 2087, 2021, doi: [10.1038/s41467-021-22429-0](https://doi.org/10.1038/s41467-021-22429-0).
- [58] X. Chu and A. Dalgarno, "Linear response time-dependent density functional theory for van der Waals coefficients," *The journal of chemical physics*, vol. 121, no. 9, pp. 4083–4088, 2004, doi: [10.1063/1.1779576](https://doi.org/10.1063/1.1779576).
- [59] K. T. Tang, J. M. Norbeck, and P. R. Certain, "Upper and lower bounds of two- and three-body dipole, quadrupole, and octupole van der Waals coefficients for hydrogen, noble gas, and alkali atom interactions," *The journal of chemical physics*, vol. 64, no. 7, pp.

- 3063–3074, 1976, doi: [10.1063/1.432569](https://doi.org/10.1063/1.432569).
- [60] J. C. Slater, “Atomic Radii in Crystals,” *The journal of chemical physics*, vol. 41, no. 10, pp. 3199–3204, 1964, doi: [10.1063/1.1725697](https://doi.org/10.1063/1.1725697).
- [61] B. Cordero *et al.*, “Covalent radii revisited,” *Dalton transactions*, no. 21, pp. 2832–2838, 2008, doi: [10.1039/B801115J](https://doi.org/10.1039/B801115J).
- [62] P. Pyykkö and M. Atsumi, “Molecular Single-Bond Covalent Radii for Elements 1–118,” *Chemistry a european journal*, vol. 15, no. 1, pp. 186–197, 2009, doi: [10.1002/chem.200800987](https://doi.org/10.1002/chem.200800987).
- [63] P. Schwerdtfeger and J. K. Nagle, “2018 Table of static dipole polarizabilities of the neutral elements in the periodic table,” *Molecular physics*, vol. 117, no. 9–12, pp. 1200–1225, 2019, doi: [10.1080/00268976.2018.1535143](https://doi.org/10.1080/00268976.2018.1535143).
- [64] A. L. Allred and E. G. Rochow, “A scale of electronegativity based on electrostatic force,” *Journal of inorganic and nuclear chemistry*, vol. 5, no. 4, pp. 264–268, 1958, doi: [10.1016/0022-1902\(58\)80003-2](https://doi.org/10.1016/0022-1902(58)80003-2).
- [65] T. L. Cottrell, L. E. Sutton, and M. G. Evans, “Covalency, electrovalency and electronegativity,” *Proceedings of the royal society of london. series a. mathematical and physical sciences*, vol. 207, no. 1088, pp. 49–63, 1997, doi: [10.1098/rspa.1951.0098](https://doi.org/10.1098/rspa.1951.0098).
- [66] W. Gordy, “A New Method of Determining Electronegativity from Other Atomic Properties,” *Physical review*, vol. 69, no. 11–12, pp. 604–607, 1946, doi: [10.1103/PhysRev.69.604](https://doi.org/10.1103/PhysRev.69.604).
- [67] D. C. Ghosh, “A new scale of electronegativity based on absolute radii of atoms,” *Journal of theoretical and computational chemistry*, vol. 04, no. 01, pp. 21–33, 2005, doi: [10.1142/S0219633605001556](https://doi.org/10.1142/S0219633605001556).
- [68] S. S. Batsanov, “Dielectric Methods of Studying the Chemical Bond and the Concept of Electronegativity,” *Russian chemical reviews*, vol. 51, no. 7, p. 684, 1982, doi: [10.1070/RC1982v051n07](https://doi.org/10.1070/RC1982v051n07).
- [69] J. K. Nagle, “Atomic polarizability and electronegativity,” *Journal of the american chemical society*, vol. 112, no. 12, pp. 4741–4747, 1990, doi: [10.1021/ja00168a019](https://doi.org/10.1021/ja00168a019).
- [70] H. Glawe, A. Sanna, E. K. U. Gross, and M. A. L. Marques, “The optimal one dimensional periodic table: A modified Pettifor chemical scale from data mining,” *New journal of physics*, vol. 18, no. 9, p. 093011, 2016, doi: [10.1088/1367-2630/18/9/093011](https://doi.org/10.1088/1367-2630/18/9/093011).
- [71] D. G. Pettifor, “A chemical scale for crystal-structure maps,” *Solid state communications*, vol. 51, no. 1, pp. 31–34, 1984, doi: [10.1016/0038-1098\(84\)90765-8](https://doi.org/10.1016/0038-1098(84)90765-8).
- [72] P. Villars, K. Cenzual, J. Daams, Y. Chen, and S. Iwata, “Data-driven atomic environment prediction for binaries using the Mendeleev number: Part 1. Composition AB,” *Journal of alloys and compounds*, vol. 367, no. 1, pp. 167–175, 2004, doi: [10.1016/j.jallcom.2003.08.060](https://doi.org/10.1016/j.jallcom.2003.08.060).
- [73] S. Alvarez, “A cartography of the van der Waals territories,” *Dalton transactions*, vol. 42, no. 24, pp. 8617–8636, 2013, doi: [10.1039/C3DT50599E](https://doi.org/10.1039/C3DT50599E).
- [74] N. L. Allinger, X. Zhou, and J. Bergsma, “Molecular mechanics parameters,” *Journal of molecular structure: Theochem*, vol. 312, no. 1, pp. 69–83, 1994, doi: [10.1016/S0166-1280\(09\)80008-0](https://doi.org/10.1016/S0166-1280(09)80008-0).

Tables and figures

Table 1: Meaning and units of some symbols used in this work. Reference for the glass and melt data is the SciGlass database, and references for the physicochemical data are given in the table.

Symbol	Meaning
T	Temperature (K)
η	Equilibrium shear viscosity (Pa.s)
T_n ($n \in \mathbb{Z}$)	Temperature (K) where $\eta = 10^n$ Pa.s
T_g	Glass transition temperature (K)
T_{melt}	Melting temperature (K)
T_{liq}	Liquidus temperature (K)
T_{Lit}	Littleton softening point (K)
T_{ann}	Annealing point (K)
T_{strain}	Strain point (K)
T_{soft}	Softening point (K)
T_{dil}	Dilatometric softening temperature (K)
V_D	Abbe's number
n_D	Refractive index
n (low)	Refractive index measured at a wavelength between 0.6 and 1 micron at 293 K
n (high)	Refractive index measured at a wavelength greater than 1 micron at 293 K
$n_F - n_C$	Mean dispersion
ε	Relative permittivity at ambient temperature and frequency of 1 MHz
$T_{\rho=10^6 \Omega.m}$	Temperature (K) where the specific electrical resistivity is 10^6 $\Omega.m$
ρ	Specific electrical resistivity ($\Omega.m$)
E	Young's modulus (GPa)
G	Shear modulus (GPa)
H	Microhardness measured by Knoop or Vickers indentation (GPa)
ν	Poisson's ratio
D	Density (g.cm^{-3})
κ	Thermal conductivity ($\text{W.m}^{-1}\text{.K}^{-1}$)
ΔT	Thermal shock resistance (K)
α_L	Linear coefficient of thermal expansion (K^{-1})
C_p	Heat capacity at constant pressure ($\text{J}.\text{kg}^{-1}.\text{K}^{-1}$)

Continued on next page

Continued from previous page

Symbol	Meaning
$T_{\max(U)}$	Temperature (K) of maximum crystal growth velocity
U_{\max}	Maximum crystal growth velocity ($\text{m} \cdot \text{s}^{-1}$)
T_c	Temperature (K) of the crystallization peak (differential thermal analysis)
T_x	Temperature (K) of the crystallization onset (differential thermal analysis)
γ	Surface tension ($\text{J} \cdot \text{m}^{-2}$)
r_W	Van der Walls radius (pm) [51]
r_R	Atomic radius (pm) [52]
V_{at}	Atomic volume ($\text{cm}^3 \cdot \text{mol}^{-1}$) [30]
E_{ea}	Electron affinity (eV) [53], [54]
E_g	DFT bandgap energy of $T = 0$ K ground state (eV) [26]
E_{at}	DFT energy per atom of $T = 0$ K ground state ($\text{eV} \cdot \text{atom}^{-1}$) [26]
m_m	DFT magnetic moment of $T = 0$ K ground state [26]
FCC_{lp}	Estimated FCC lattice parameter based on the DFT volume of the OQMD ground state [26]
Z_{eff}	Effective nuclear charge [30]
χ_S	Electronegativity in the Sanderson scale [55], [56]
χ_{TO}	Electronegativity in the Tardini-Organov scale [57]
T_b	Boiling point (K) [53]
ΔH_m	Melting Enthalpy ($\text{kJ} \cdot \text{mol}^{-1}$) [26]
C_6	C_6 coefficient (a.u) [58], [59]
N_v	Number of valence electrons [30]
N_{ox}	Number of oxidation states [30]
N_u	Number of unfilled valence orbitals [26]
$N_{u,s}$	Number of unfilled s valence orbitals [26]
$N_{u,p}$	Number of unfilled p valence orbitals [26]
$N_{u,d}$	Number of unfilled d valence orbitals [26]
$N_{u,f}$	Number of unfilled f valence orbitals [26]
$N_{f,s}$	Number of filled s valence orbitals [26]
$N_{f,p}$	Number of filled p valence orbitals [26]
$N_{f,d}$	Number of filled d valence orbitals [26]

Continued on next page

Continued from previous page

Symbol

Meaning

$N_{f,f}$

Number of filled f valence orbitals [26]

Table 2: Search space used during hyperparameter tuning and selected hyperparameter values. The learning rate values were drawn in logarithmic space instead of linear space to sample the entire interval uniformly.

Hyperparameter	Search space	Selected
Number of layers	{1, 2, 3, 4, 5}	4
Number of neurons in layer 1	{10, 20, ..., 500}	280
Number of neurons in layer 2	{10, 20, ..., 500}	500
Number of neurons in layer 3	{10, 20, ..., 500}	390
Number of neurons in layer 4	{10, 20, ..., 500}	480
Number of neurons in layer 5	{10, 20, ..., 500}	—
Activation function of layer 1	See text	Softplus
Activation function of layer 2	See text	Mish
Activation function of layer 3	See text	Leaky ReLu
Activation function of layer 4	See text	PReLU
Activation function of layer 5	See text	—
Use batch normalization in layer 1	{true, false}	true
Use batch normalization in layer 2	{true, false}	true
Use batch normalization in layer 3	{true, false}	false
Use batch normalization in layer 4	{true, false}	false
Use batch normalization in layer 5	{true, false}	—
Dropout percentage in layer 1	[0, 0.5]	0.081
Dropout percentage in layer 2	[0, 0.5]	0.001
Dropout percentage in layer 3	[0, 0.5]	0.087
Dropout percentage in layer 4	[0, 0.5]	0.168
Dropout percentage in layer 5	[0, 0.5]	—
Learning rate	$[10^{-5}, 10^{-1}]$	1.33×10^{-5}
Batch size	{256, 512, 1024, 2048, 4096}	256
Early stopping patience	{5, 6, ..., 35}	27

Table 3: Descriptive statistics and metrics (RMSE, see text) for all the properties studied in this work. The lower the RMSE, the better. The last three columns show the results of the t-test (95% confidence) used to compare the performance of the models. In these columns, MLP means that the multilayer perceptron model performed better, MH means that the multi-headed model performed better, RF means that the random forest model performed better, and = means that no statistical difference was observed.

Symbol	Count	Min	Mean	Max	RMSE (MLP)	RMSE (MH)	RMSE (RF)	MLP vs. MH	MLP vs. RF	MH vs. RF
T_0	1598	412	1520	2620	100(20)	90(20)	120(20)	=	MLP	MH
T_1	7043	373	1620	2500	70(10)	65(8)	68(6)	=	=	=
T_2	14250	391	1540	2500	48(6)	43(5)	55(4)	=	MLP	MH
T_3	13216	358	1380	2240	51(4)	48(5)	56(4)	=	MLP	MH
T_4	7375	344	1240	1800	44(7)	40(10)	58(7)	=	MLP	MH
T_5	5452	334	1060	2210	39(9)	37(7)	50(10)	=	MLP	MH
T_6	4790	326	973	2040	40(7)	39(5)	50(10)	=	MLP	MH
T_7	4977	318	907	1900	37(5)	34(3)	45(6)	=	MLP	MH
T_8	5158	310	870	1770	35(3)	34(3)	50(6)	=	MLP	MH
T_9	5561	303	847	1690	32(3)	31(2)	57(4)	=	MLP	MH
T_{10}	5899	296	827	1640	31(3)	32(3)	58(4)	=	MLP	MH
T_{11}	5589	290	806	1650	33(3)	31(3)	58(5)	=	MLP	MH
T_{12}	4357	281	779	1520	32(4)	32(4)	52(3)	=	MLP	MH
$\log_{10}(\eta(773\text{ K}))$	1838	-0.977	8.46	12.5	1.1(2)	1.0(3)	1.3(2)	=	MLP	MH
$\log_{10}(\eta(873\text{ K}))$	3217	-0.676	7.88	12.5	0.8(1)	0.8(2)	1.0(1)	=	MLP	MH
$\log_{10}(\eta(973\text{ K}))$	3703	-0.945	6.42	12.5	0.73(6)	0.71(7)	0.85(7)	=	MLP	MH
$\log_{10}(\eta(1073\text{ K}))$	4121	-0.919	5.27	12.5	0.59(7)	0.55(6)	0.70(9)	=	MLP	MH
$\log_{10}(\eta(1173\text{ K}))$	4612	-0.98	4.2	12.4	0.48(6)	0.46(4)	0.51(7)	=	=	=
$\log_{10}(\eta(1273\text{ K}))$	5551	-0.901	3.4	12.4	0.44(4)	0.43(5)	0.47(8)	=	=	=
$\log_{10}(\eta(1373\text{ K}))$	7130	-0.966	2.84	12.4	0.33(3)	0.32(4)	0.39(6)	=	MLP	MH
$\log_{10}(\eta(1473\text{ K}))$	9426	-0.882	2.52	12.5	0.28(2)	0.28(3)	0.36(4)	=	MLP	MH
$\log_{10}(\eta(1573\text{ K}))$	10576	-1	2.09	11.8	0.24(1)	0.23(2)	0.27(4)	=	MLP	MH
$\log_{10}(\eta(1673\text{ K}))$	10285	-0.955	1.71	10.8	0.24(1)	0.23(2)	0.25(6)	=	=	=
$\log_{10}(\eta(1773\text{ K}))$	7577	-0.996	1.48	7.92	0.21(2)	0.21(2)	0.21(6)	=	=	=
$\log_{10}(\eta(1873\text{ K}))$	4117	-0.983	1.37	7.21	0.23(3)	0.21(3)	0.22(4)	=	=	=
$\log_{10}(\eta(2073\text{ K}))$	172	-0.976	0.844	5.8	0.2(2)	0.2(2)	0.3(3)	=	=	=

Continued from previous page

Symbol	Count	Min	Mean	Max	RMSE (MLP)	RMSE (MH)	RMSE (RF)	MLP vs. MH	MLP vs. RF	MH vs. RF
$\log_{10}(\eta(2273\text{K}))$	44	-0.984	0.452	4.56	0.2(5)	0.2(5)	0.4(6)	=	=	=
$\log_{10}(\eta(2473\text{K}))$	17	-0.998	0.494	3.67	0.1(6)	0(1)	0.5(8)	=	=	=
T_g	73504	213	713	1460	48(1)	45(1)	34(1)	MH	RF	RF
T_{melt}	15552	160	1040	3230	115(8)	99(5)	73(8)	MH	RF	RF
T_{liq}	40260	303	1340	3090	99(4)	86(2)	53(3)	MH	RF	RF
T_{Lit}	4226	533	979	1890	31(4)	30(5)	34(7)	=	=	=
T_{ann}	8292	334	918	1400	21(1)	20(2)	21(4)	=	=	=
T_{strain}	10377	332	884	1390	24(2)	23(2)	20(5)	=	RF	=
T_{soft}	12815	311	926	1520	45(4)	42(4)	40(4)	=	RF	=
T_{dil}	18312	284	819	1420	44(2)	40(1)	39(1)	MH	RF	RF
V_D	26019	7.94	46.3	110	3.3(3)	2.8(2)	2.3(2)	MH	RF	RF
n_D	54442	1.12	1.68	3.87	0.059(5)	0.052(4)	0.039(4)	MH	RF	RF
n (low)	359	1.43	2.35	3.11	0.13(4)	0.12(4)	0.11(4)	=	=	=
n (high)	410	1.9	2.56	3.5	0.09(1)	0.08(2)	0.10(2)	=	=	MLP
$\log_{10}(n_F - n_C)$	25873	-2.8	-1.79	-0.749	0.044(5)	0.040(5)	0.035(5)	=	RF	RF
ε	3113	1.74	10.3	50	2.2(3)	2.1(4)	2.4(4)	=	=	=
$\log_{10}(\tan(\delta))$	2335	-4	-2.6	-0.815	0.18(2)	0.20(3)	0.18(3)	=	=	=
$T_{\rho=10^6 \Omega.m}$	12592	0.15	473	1580	65(4)	63(4)	60(5)	=	RF	=
$\log_{10}(\rho(273\text{K}))$	13130	-28.2	4.98	31.2	2.5(2)	2.3(2)	1.9(2)	MH	RF	RF
$\log_{10}(\rho(373\text{K}))$	13681	-29.2	3.8	26.3	2.2(2)	2.1(2)	1.7(2)	=	RF	RF
$\log_{10}(\rho(423\text{K}))$	14499	-26.6	3.54	24.6	2.1(1)	2.0(2)	1.8(2)	=	RF	RF
$\log_{10}(\rho(573\text{K}))$	11351	-21.7	2.66	17.2	1.89(7)	1.82(9)	1.5(2)	=	RF	RF
$\log_{10}(\rho(1073\text{K}))$	1880	-8.3	-2.78	3.73	0.32(6)	0.33(7)	0.42(9)	=	MLP	MH
$\log_{10}(\rho(1273\text{K}))$	2334	-8	-3.16	4.09	0.65(8)	0.7(1)	0.7(1)	=	=	=
$\log_{10}(\rho(1473\text{K}))$	2074	-8.05	-3.24	4.16	1.10(4)	1.09(9)	1.15(7)	=	=	=
$\log_{10}(\rho(1673\text{K}))$	2086	-7.74	-3.44	3.73	0.76(7)	0.72(7)	0.77(8)	=	=	=
E	14476	1.62	74.5	175	7.5(5)	6.9(5)	6.6(5)	MH	RF	=
G	6733	1.37	25.6	72	3.4(4)	3.2(4)	3.2(4)	=	=	=
H	13842	0.0024	4.2	14.7	0.85(6)	0.80(6)	0.65(5)	=	RF	RF
ν	6491	0.052	0.256	0.821	0.037(3)	0.037(3)	0.035(4)	=	=	=

Continued on next page

Continued from previous page

Symbol	Count	Min	Mean	Max	RMSE (MLP)	RMSE (MH)	RMSE (RF)	MLP vs. MH	MLP vs. RF	MH vs. RF
$D(293\text{ K})$	80509	1.14	3.49	9.94	0.322(9)	0.286(8)	0.22(1)	MH	RF	RF
$D(1073\text{ K})$	808	1.53	3.62	9.79	0.3(1)	0.39(8)	0.30(9)	MLP	=	RF
$D(1273\text{ K})$	995	1.41	3.2	8.17	0.22(3)	0.21(3)	0.28(5)	=	MLP	MH
$D(1473\text{ K})$	843	1.5	3.14	7.62	0.12(3)	0.13(3)	0.16(6)	=	=	=
$D(1673\text{ K})$	840	1.35	2.9	4.85	0.13(3)	0.14(3)	0.17(3)	=	MLP	MH
κ	1246	0.002	0.832	5.94	0.5(1)	0.5(1)	0.4(2)	=	=	=
ΔT	1058	25	175	1000	50(10)	38(9)	50(20)	MH	=	=
$\log_{10}(\alpha_L(T < T_g))$	59351	-8	-5.1	-3.75	0.073(3)	0.073(3)	0.058(4)	=	RF	RF
$\log_{10}(\alpha_L(328\text{ K}))$	2220	-6.48	-5.07	-4	0.062(8)	0.06(1)	0.08(1)	=	MLP	MH
$\log_{10}(\alpha_L(373\text{ K}))$	2300	-6.41	-4.99	-3.95	0.08(2)	0.08(2)	0.10(2)	=	MLP	MH
$\log_{10}(\alpha_L(433\text{ K}))$	17600	-7.7	-5.14	-3.89	0.060(5)	0.063(5)	0.047(4)	=	RF	RF
$\log_{10}(\alpha_L(483\text{ K}))$	14618	-6.81	-5.13	-3.85	0.047(3)	0.043(3)	0.049(6)	MH	=	MH
$\log_{10}(\alpha_L(623\text{ K}))$	1164	-7.32	-5.13	-3.75	0.09(2)	0.09(2)	0.13(4)	=	MLP	MH
$C_p(293\text{ K})$	710	0.392	671	1560	140(30)	140(40)	160(30)	=	=	=
$C_p(473\text{ K})$	652	0.495	793	1900	150(50)	160(50)	170(60)	=	=	=
$C_p(673\text{ K})$	499	2.63	1000	2460	160(20)	170(40)	160(50)	=	=	=
$C_p(1073\text{ K})$	297	524	1350	2220	180(20)	180(20)	220(30)	=	MLP	MH
$C_p(1273\text{ K})$	181	748	1430	2790	300(200)	300(200)	300(100)	=	=	=
$C_p(1473\text{ K})$	167	765	1450	2620	390(50)	400(50)	410(60)	=	=	=
$C_p(1673\text{ K})$	116	781	1390	2050	70(50)	60(50)	60(60)	=	=	=
$T_{\max(U)}$	788	592	1210	1820	70(10)	70(10)	70(20)	=	=	=
$\log_{10}(U_{\max})$	775	-9.85	-7.34	-2.53	0.6(1)	0.6(1)	0.6(1)	=	=	=
T_c	20049	263	838	1630	74(3)	69(3)	51(3)	MH	RF	RF
T_x	11688	297	789	1810	58(3)	54(3)	44(3)	MH	RF	RF
$\gamma(T > T_g)$	3584	0.0439	0.319	0.79	0.040(3)	0.038(4)	0.041(5)	=	=	=
$\gamma(1173\text{ K})$	707	0.0613	0.182	0.425	0.014(4)	0.013(6)	0.017(4)	=	=	=
$\gamma(1473\text{ K})$	877	0.0483	0.226	0.456	0.030(2)	0.028(3)	0.033(3)	=	MLP	MH
$\gamma(1573\text{ K})$	1187	0.0856	0.277	0.619	0.029(2)	0.027(3)	0.031(3)	=	=	MH
$\gamma(1673\text{ K})$	760	0.0851	0.364	0.632	0.043(5)	0.044(4)	0.044(6)	=	=	=

Table 4: Descriptive statistics of the chemical elements present in the entire dataset (before the holdout split). All values (except the second column) are rounded to the third decimal place. SD is the standard deviation, and Q_1 and Q_3 are the first and third quartiles, respectively.

Element	Count	Mean	SD	Q_1	Median	Q_3	Maximum
Re	1	0.001	—	0.001	0.001	0.001	0.001
Pd	4	0.002	0.001	0.001	0.002	0.002	0.003
Ru	15	0.003	0.002	0.002	0.003	0.004	0.007
Au	19	0.015	0.028	0.001	0.003	0.006	0.1
C	249	0.03	0.043	0.003	0.015	0.041	0.367
Lu	257	0.054	0.062	0.005	0.029	0.089	0.4
Sc	333	0.054	0.064	0.013	0.032	0.07	0.4
Tm	488	0.009	0.017	0.001	0.003	0.007	0.167
Hg	501	0.098	0.085	0.037	0.082	0.132	0.5
Ho	511	0.042	0.078	0.003	0.006	0.044	0.4
Tb	609	0.049	0.06	0.005	0.03	0.076	0.4
Eu	830	0.024	0.05	0.003	0.005	0.016	0.4
Hf	915	0.077	0.067	0.014	0.059	0.138	0.333
Dy	924	0.053	0.08	0.003	0.008	0.08	0.4
Sm	1136	0.032	0.058	0.003	0.007	0.032	0.4
Pr	1228	0.033	0.063	0.003	0.006	0.029	0.4
Ni	1264	0.024	0.063	0.002	0.004	0.018	0.5
Co	1377	0.038	0.064	0.003	0.01	0.044	0.5
N	1570	0.068	0.065	0.02	0.052	0.087	0.438
H	1598	0.063	0.078	0.01	0.037	0.08	0.559
Rb	1931	0.135	0.112	0.05	0.107	0.191	1
Cr	2120	0.037	0.059	0.002	0.009	0.039	0.4
Br	2267	0.228	0.245	0.02	0.1	0.5	0.8
Be	2347	0.123	0.097	0.045	0.091	0.19	0.5
Yb	2392	0.022	0.039	0.004	0.008	0.025	0.5
In	2655	0.075	0.089	0.02	0.052	0.1	1
Er	2780	0.022	0.052	0.002	0.004	0.011	0.4
Cs	3302	0.106	0.108	0.025	0.073	0.155	1
Tl	3304	0.168	0.16	0.05	0.12	0.235	1
Nd	3389	0.028	0.053	0.003	0.006	0.026	0.4
Ce	3641	0.019	0.042	0.001	0.004	0.02	0.5
Mo	4068	0.084	0.07	0.015	0.069	0.149	0.25
I	4396	0.148	0.139	0.05	0.105	0.2	1
Sn	4809	0.067	0.092	0.002	0.021	0.116	1
Cd	5012	0.07	0.077	0.017	0.044	0.096	0.993
Mn	5294	0.049	0.065	0.004	0.021	0.068	0.5
Cu	5596	0.072	0.108	0.006	0.023	0.095	0.928
Ta	5903	0.022	0.03	0.007	0.015	0.025	0.286
Ga	6106	0.104	0.098	0.04	0.08	0.133	1
Ag	6126	0.182	0.144	0.062	0.162	0.263	1
Cl	6203	0.119	0.172	0.006	0.044	0.15	0.745
Gd	6306	0.035	0.043	0.012	0.023	0.042	0.4
Y	8075	0.032	0.041	0.008	0.018	0.04	0.4
W	8175	0.034	0.045	0.006	0.014	0.042	0.25

Continued on next page

Continued from previous page

Element	Count	Mean	SD	Q ₁	Median	Q ₃	Maximum
V	8710	0.13	0.079	0.059	0.138	0.193	0.287
Sb	8998	0.079	0.118	0.001	0.011	0.12	1
Se	9705	0.522	0.22	0.4	0.565	0.65	1
S	10870	0.328	0.269	0.014	0.384	0.581	1
As	11904	0.176	0.169	0.002	0.15	0.318	1
Bi	12245	0.117	0.097	0.033	0.095	0.182	1
Nb	13397	0.051	0.054	0.012	0.031	0.076	0.286
Fe	14397	0.05	0.074	0.003	0.02	0.066	0.5
Te	15351	0.24	0.199	0.099	0.204	0.286	1
Ge	16506	0.176	0.112	0.09	0.175	0.246	1
La	19465	0.049	0.045	0.012	0.041	0.074	0.4
Sr	20495	0.029	0.037	0.006	0.016	0.036	0.5
Zr	24871	0.026	0.041	0.005	0.011	0.02	0.333
Pb	25993	0.096	0.087	0.032	0.074	0.139	1
F	26165	0.304	0.279	0.043	0.197	0.61	0.833
Ti	27353	0.038	0.052	0.006	0.017	0.049	0.357
Zn	37706	0.048	0.047	0.014	0.033	0.068	0.5
P	39374	0.138	0.08	0.075	0.15	0.2	1
Li	39671	0.082	0.081	0.025	0.055	0.111	0.667
Mg	43682	0.034	0.036	0.012	0.021	0.044	0.5
Ba	44149	0.043	0.044	0.011	0.028	0.063	1
K	47969	0.055	0.068	0.011	0.032	0.068	0.667
Ca	62503	0.055	0.057	0.017	0.034	0.078	0.5
Na	77163	0.082	0.068	0.033	0.068	0.109	0.667
B	80769	0.138	0.102	0.05	0.118	0.216	0.401
Al	85456	0.053	0.046	0.018	0.045	0.075	0.527
Si	118216	0.164	0.076	0.116	0.186	0.221	1
O	192270	0.586	0.085	0.573	0.6	0.623	0.75

Table 5: Selected physicochemical features.

Feature	Origin	Aggregator	Symbol
Atomic fraction of Ag	Glass composition	–	Ag
Atomic fraction of Al	Glass composition	–	Al
Atomic fraction of As	Glass composition	–	As
Atomic fraction of B	Glass composition	–	B
Atomic fraction of Ba	Glass composition	–	Ba
Atomic fraction of Be	Glass composition	–	Be
Atomic fraction of Bi	Glass composition	–	Bi
Atomic fraction of Br	Glass composition	–	Br
Atomic fraction of C	Glass composition	–	C
Atomic fraction of Ca	Glass composition	–	Ca
Atomic fraction of Cd	Glass composition	–	Cd
Atomic fraction of Ce	Glass composition	–	Ce
Atomic fraction of Cl	Glass composition	–	Cl
Atomic fraction of Co	Glass composition	–	Co
Atomic fraction of Cr	Glass composition	–	Cr
Atomic fraction of Cs	Glass composition	–	Cs
Atomic fraction of Cu	Glass composition	–	Cu
Atomic fraction of Dy	Glass composition	–	Dy
Atomic fraction of Er	Glass composition	–	Er
Atomic fraction of Eu	Glass composition	–	Eu
Atomic fraction of Fe	Glass composition	–	Fe
Atomic fraction of Ga	Glass composition	–	Ga
Atomic fraction of Gd	Glass composition	–	Gd
Atomic fraction of Ge	Glass composition	–	Ge
Atomic fraction of H	Glass composition	–	H
Atomic fraction of Hf	Glass composition	–	Hf
Atomic fraction of Hg	Glass composition	–	Hg
Atomic fraction of Ho	Glass composition	–	Ho
Atomic fraction of I	Glass composition	–	I

Continued on next page

Continued from previous page

Feature	Origin	Aggregator	Symbol
Atomic fraction of In	Glass composition	–	In
Atomic fraction of K	Glass composition	–	K
Atomic fraction of La	Glass composition	–	La
Atomic fraction of Li	Glass composition	–	Li
Atomic fraction of Lu	Glass composition	–	Lu
Atomic fraction of Mg	Glass composition	–	Mg
Atomic fraction of Mn	Glass composition	–	Mn
Atomic fraction of Mo	Glass composition	–	Mo
Atomic fraction of N	Glass composition	–	N
Atomic fraction of Na	Glass composition	–	Na
Atomic fraction of Nb	Glass composition	–	Nb
Atomic fraction of Nd	Glass composition	–	Nd
Atomic fraction of Ni	Glass composition	–	Ni
Atomic fraction of P	Glass composition	–	P
Atomic fraction of Pb	Glass composition	–	Pb
Atomic fraction of Pr	Glass composition	–	Pr
Atomic fraction of Rb	Glass composition	–	Rb
Atomic fraction of S	Glass composition	–	S
Atomic fraction of Sb	Glass composition	–	Sb
Atomic fraction of Sc	Glass composition	–	Sc
Atomic fraction of Se	Glass composition	–	Se
Atomic fraction of Sm	Glass composition	–	Sm
Atomic fraction of Sn	Glass composition	–	Sn
Atomic fraction of Sr	Glass composition	–	Sr
Atomic fraction of Ta	Glass composition	–	Ta
Atomic fraction of Tb	Glass composition	–	Tb
Atomic fraction of Te	Glass composition	–	Te
Atomic fraction of Ti	Glass composition	–	Ti
Atomic fraction of Tl	Glass composition	–	Tl
Atomic fraction of V	Glass composition	–	V

Continued on next page

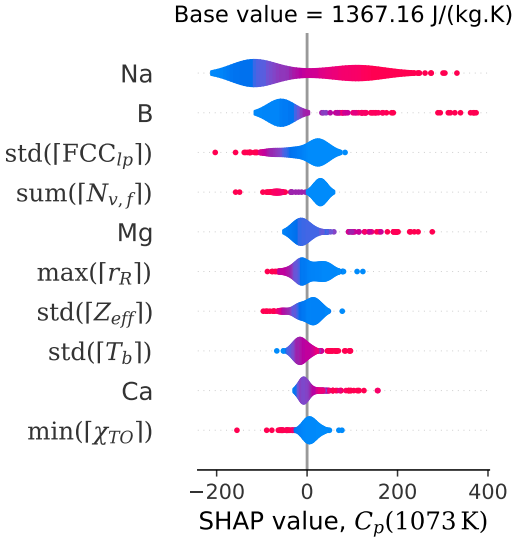
Continued from previous page

Feature	Origin	Aggregator	Symbol
Atomic fraction of W	Glass composition	–	W
Atomic fraction of Y	Glass composition	–	Y
Atomic fraction of Yb	Glass composition	–	Yb
Atomic fraction of Zn	Glass composition	–	Zn
Atomic fraction of Zr	Glass composition	–	Zr
C_6	Eq. (1)	Minimum	$\min(C_6)$
Electron affinity	Eq. (1)	Minimum	$\min(E_{ea})$
Number of unfilled valence orbitals	Eq. (1)	Standard dev.	$\text{std}(N_u)$
Number of filled d valence orbitals	Eq. (1)	Minimum	$\min(N_{f,d})$
Number of filled f valence orbitals	Eq. (1)	Minimum	$\min(N_{f,f})$
Number of unfilled p valence orbitals	Eq. (1)	Minimum	$\min(N_{u,p})$
Number of unfilled s valence orbitals	Eq. (1)	Minimum	$\min(N_{u,s})$
Number of valence electrons	Eq. (1)	Maximum	$\max(N_v)$
Atomic volume	Eq. (1)	Minimum	$\min(V_{at})$
DFT bandgap energy of $T = 0$ K ground state	Eq. (1)	Minimum	$\min(E_g)$
DFT energy per atom of $T = 0$ K ground state	Eq. (1)	Maximum	$\max(E_{at})$
Fusion Enthalpy	Eq. (1)	Minimum	$\min(\Delta H_m)$
Number of oxidation states	Eq. (2)	Maximum	$\max([N_{ox}])$
Number of unfilled valence orbitals	Eq. (2)	Minimum	$\min([N_u])$
Number of unfilled d valence orbitals	Eq. (2)	Maximum	$\max([N_{u,d}])$
Number of filled d valence orbitals	Eq. (2)	Maximum	$\max([N_{f,d}])$
Number of unfilled f valence orbitals	Eq. (2)	Sum	$\text{sum}([N_{u,f}])$
Number of filled f valence orbitals	Eq. (2)	Sum	$\text{sum}([N_f])$
Number of unfilled p valence orbitals	Eq. (2)	Sum	$\text{sum}([N_{u,p}])$
Number of unfilled p valence orbitals	Eq. (2)	Maximum	$\max([N_{u,p}])$
Number of filled p valence orbitals	Eq. (2)	Maximum	$\max([N_{f,p}])$
Number of unfilled s valence orbitals	Eq. (2)	Sum	$\text{sum}([N_{u,s}])$
Number of filled s valence orbitals	Eq. (2)	Minimum	$\min([N_{f,s}])$
Number of valence electrons	Eq. (2)	Maximum	$\max([N_v])$
Van der Walls radius	Eq. (2)	Maximum	$\max([r_W])$

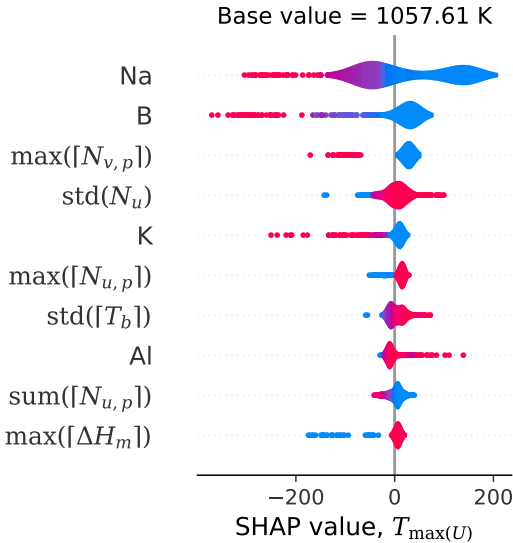
Continued on next page

Continued from previous page

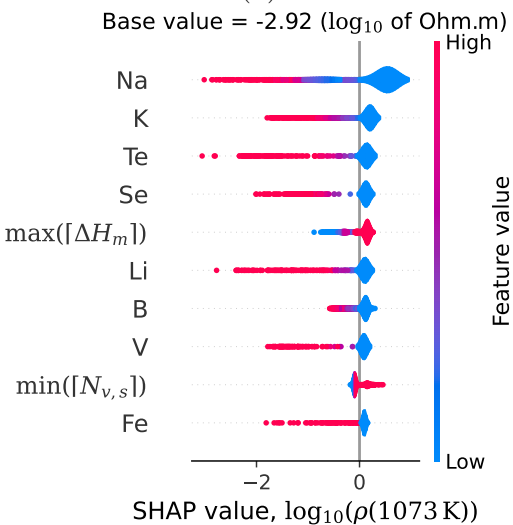
Feature	Origin	Aggregator	Symbol
Atomic radius (Rahm)	Eq. (2)	Maximum	$\max([r_R])$
DFT bandgap energy of $T = 0$ K ground state	Eq. (2)	Minimum	$\min([E_g])$
FCC lattice parameter	Eq. (2)	Standard dev.	$\text{std}([\text{FCC}_{lp}])$
DFT magnetic moment of $T = 0$ K ground state	Eq. (2)	Sum	$\text{sum}([m_m])$
Electronegativity in the Sanderson scale	Eq. (2)	Maximum	$\max([\chi_S])$
Electronegativity in the Tardini-Organov scale	Eq. (2)	Minimum	$\min([\chi_{TO}])$
Effective nuclear charge	Eq. (2)	Standard dev.	$\text{std}([Z_{\text{eff}}])$
Boiling point	Eq. (2)	Standard dev.	$\text{std}([T_b])$
Fusion Enthalpy	Eq. (2)	Maximum	$\max([\Delta H_m])$



(a)



(b)



(c)

Figure 1: Violin plots of the SHAP values for (a) $C_p(1073 \text{ K})$, (b) $T_{\max(U)}$, and (c) $\log_{10}(\rho(1073 \text{ K}))$. The color bar legend is only shown in (c), but is the same for (a) and (b).

Table 6: The most frequent SHAP features (overall and for property groups), taking into account the top 10 features for each studied property.

Overall	Viscosity and relaxation	Optical	Electrical and dielectric	Mechanical	Density	Thermal	Crystallization	Surface tension
Na	B	Pb	Na	$N_{u,s}$	$N_{f,d}$	Na	$N_{f,p}$	Ca
B	Na	N_u	$N_{f,s}$	Na	N_u	FCC _{lp}	$N_{u,p}$	B
Pb	Al	Bi	Li	ΔH_m	r_R	B	ΔH_m	r_R
Li	K	$N_{f,d}$	B	FCC _{lp}	B	Ba	B	FCC _{lp}
Al	Li	$N_{f,p}$	ΔH_m	P	Pb	Ca	Na	Na
K	Pb	Ti	Se	Mg	Na	Pb	Se	Fe
ΔH_m	$N_{f,s}$	Nb	V	Ca	$N_{f,f}$	K	S	Ba
Ca	Ca	$N_{f,f}$	Fe	r_R	Ge	$N_{f,d}$	Te	$N_{f,d}$
N_u	ΔH_m	La	K	$N_{f,d}$	Bi	P	T_b	N_u
$N_{f,d}$	P	Ge	Ag	Al	Li	Li	V	Al

Supplementary material

Data processing

Table S.7 shows the minimum and maximum values accepted for some of the properties studied in this work, as described in the Materials and Methods section of the manuscript. These values were chosen after looking at the histogram of the properties to avoid values that are unreasonably extreme (probably due to measurement or typing errors).

Table S.7: Minimum and maximum accepted values for some of the properties studied in this work. Properties not included in this list were not subjected to this restriction.

Property	Minimum	Maximum
T_3	—	2350
T_4	—	2000
$\log_{10}(\eta(1773\text{ K}))$	—	10
$\log_{10}(\eta(1873\text{ K}))$	—	10
$\log_{10}(\eta(2073\text{ K}))$	—	8
$\log_{10}(\eta(2273\text{ K}))$	—	8
T_{soft}	—	1600
V_D	—	115
n_D	—	4
n (high)	1.7	3.5
ε	—	50
$\log_{10}(\tan(\delta))$	-4	-0.796
$T_{\rho=10^6\Omega.m}$	—	2000
$\log_{10}(\rho(273\text{ K}))$	—	40
$\log_{10}(\rho(373\text{ K}))$	—	28
$\log_{10}(\rho(1073\text{ K}))$	—	4
$\log_{10}(\rho(1273\text{ K}))$	—	5
E	—	175
H	—	15
ν	—	1
$D(293\text{ K})$	1	10
κ	—	6
$\log_{10}(\alpha_L(328\text{ K}))$	-6.5	—
$\log_{10}(\alpha_L(373\text{ K}))$	-6.5	—
$\log_{10}(\alpha_L(433\text{ K}))$	-8	—
$\log_{10}(\alpha_L(483\text{ K}))$	-7	—
$C_p(293\text{ K})$	—	2000
$C_p(473\text{ K})$	—	2000
$C_p(673\text{ K})$	—	3000
$C_p(1073\text{ K})$	500	2500
$C_p(1273\text{ K})$	500	3000
$C_p(1473\text{ K})$	500	3000
$C_p(1673\text{ K})$	500	2250
$\log_{10}(U_{\max})$	-10	—
$\gamma(T > T_g)$	—	0.8
$\gamma(1473\text{ K})$	—	0.5
$\gamma(1573\text{ K})$	—	0.7

Continued on next page

Continued from previous page		
Property	Minimum	Maximum
$\gamma(1673\text{ K})$	—	0.7

Physicochemical features considered, but not selected

The physicochemical features considered in this work that were not selected are:

- Atomic number [30]
- Atomic radius [60]
- Atomic weight [30]
- Estimated BCC lattice parameter based on the DFT volume of the OQMD ground state for each element [26]
- Covalent radius [61]
- Single bond covalent radius [62]
- Density at 295 K [53]
- Dipole polarizability [63]
- Electronegativity in the Allred and Rochow scale [64]
- Electronegativity in the Cottrell and Sutton scale [65]
- Electronegativity in the Gordy scale [66]
- Electronegativity in the Gosh scale [67]
- Electronegativity in the Martynov and Batsanov scale [68]
- Electronegativity in the Nagle scale [69]
- Energy to remove the first electron [26]
- Glawe's number [70]
- Heat of formation [53]
- Mass number of the most abundant isotope [30]
- Maximum ionization energy [30]
- Melting point [53]
- Mendeleev's number [71], [72]
- Number of electrons [30]
- Number of neutrons [30]
- Number of protons [30]
- Number of valence electrons [26]

- Pettifor's number [71]
- Van der Walls radius [53]
- Van der Walls radius [73]
- Van der Walls radius [74]
- DFT volume per atom of $T = 0$ K ground state [26]

SHAP values violin plots — viscosity and relaxation

Figures S.1 to S.35 show the violin plots of the SHAP values for the viscosity and relaxation related properties. The SHAP values were calculated using the multi-headed GlassNet model, with the exception of $\log_{10}(\eta(2473\text{ K}))$, which was calculated using the MLP model because it was not possible to run the SHAP explainer with the multi-headed model.

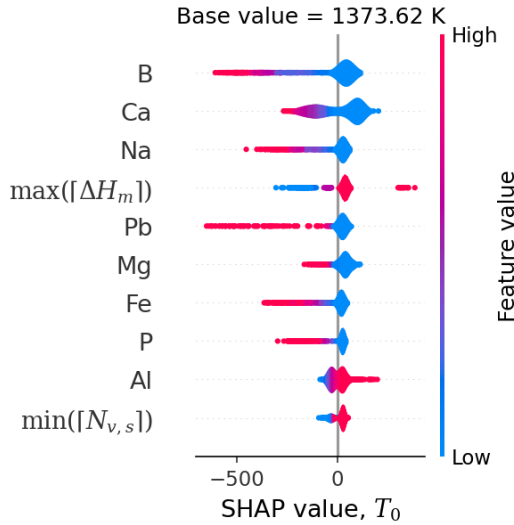


Figure S.1: Violin plot of SHAP values for T_0 .

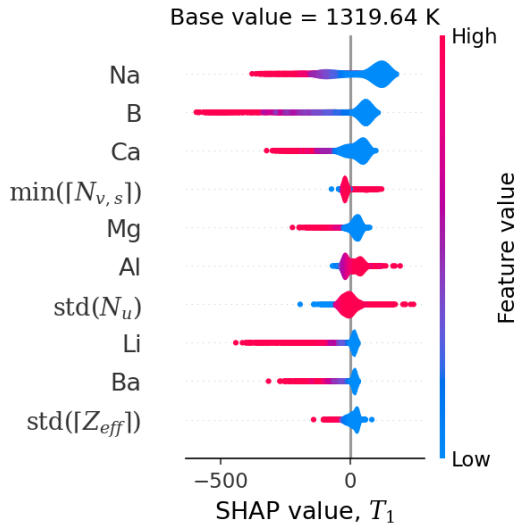


Figure S.2: Violin plot of SHAP values for T_1 .

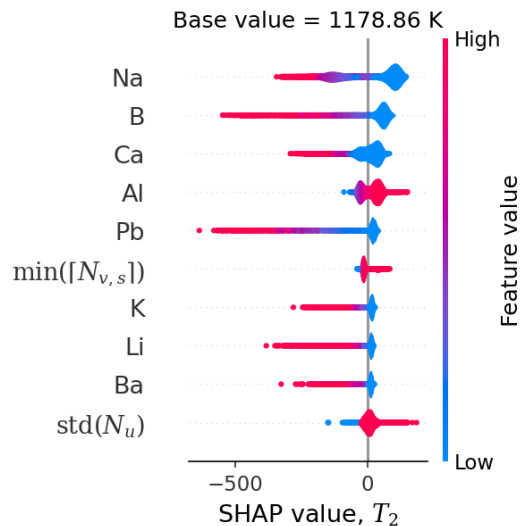


Figure S.3: Violin plot of SHAP values for T_2 .

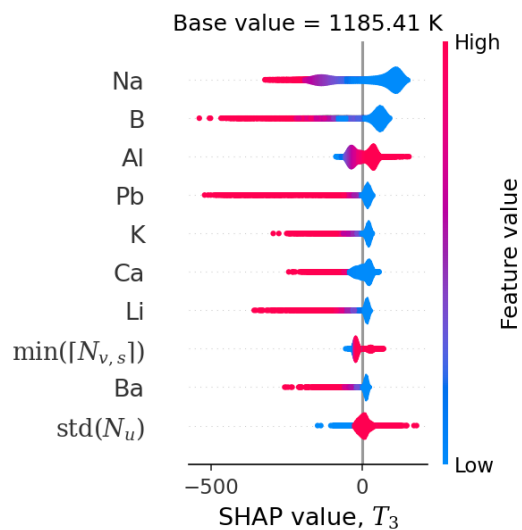


Figure S.4: Violin plot of SHAP values for T_3 .

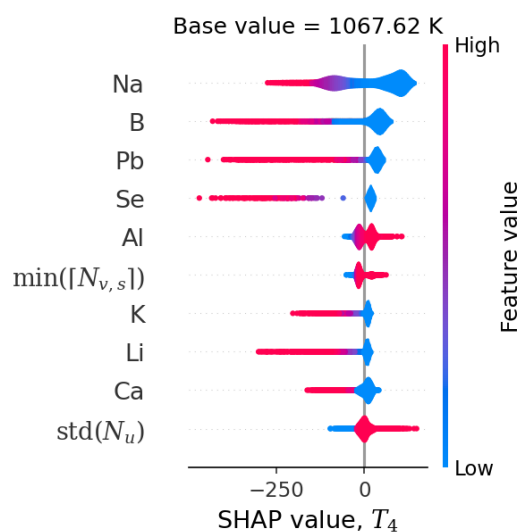


Figure S.5: Violin plot of SHAP values for T_4 .

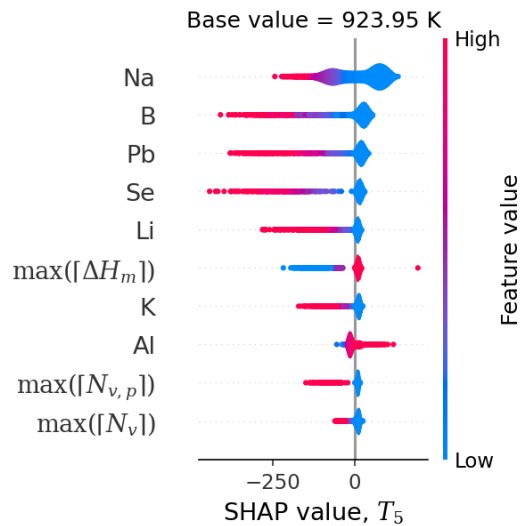


Figure S.6: Violin plot of SHAP values for T_5 .

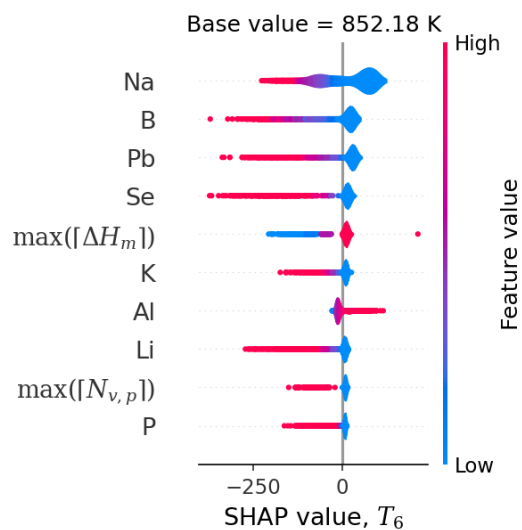


Figure S.7: Violin plot of SHAP values for T_6 .

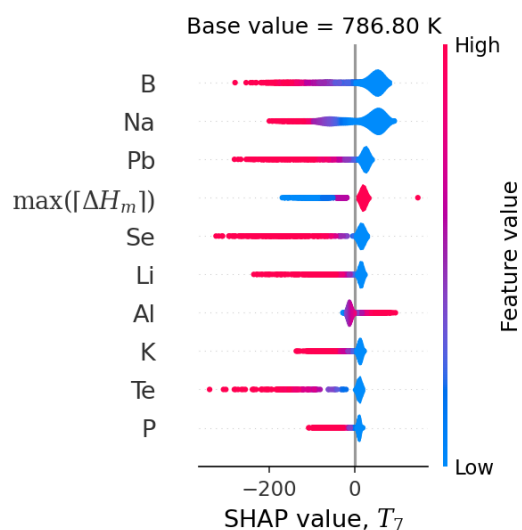


Figure S.8: Violin plot of SHAP values for T_7 .

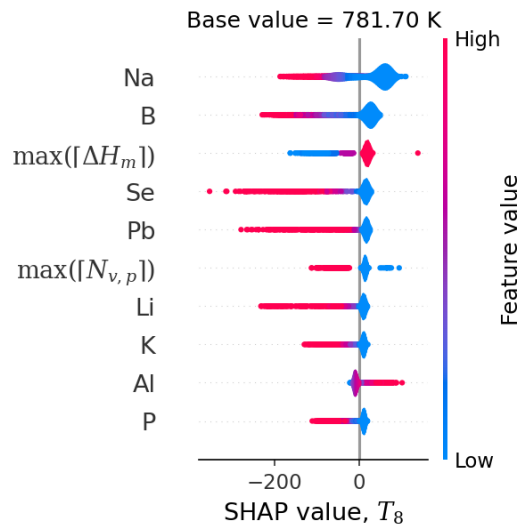


Figure S.9: Violin plot of SHAP values for T_8 .

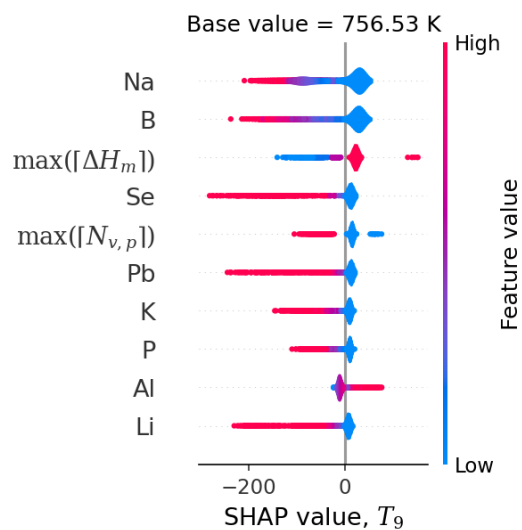


Figure S.10: Violin plot of SHAP values for T_9 .

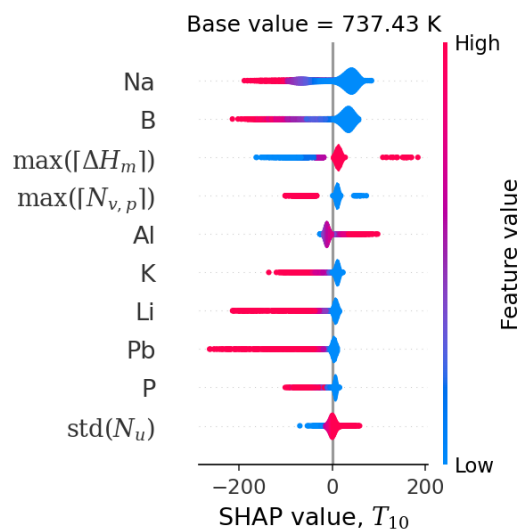


Figure S.11: Violin plot of SHAP values for T_{10} .

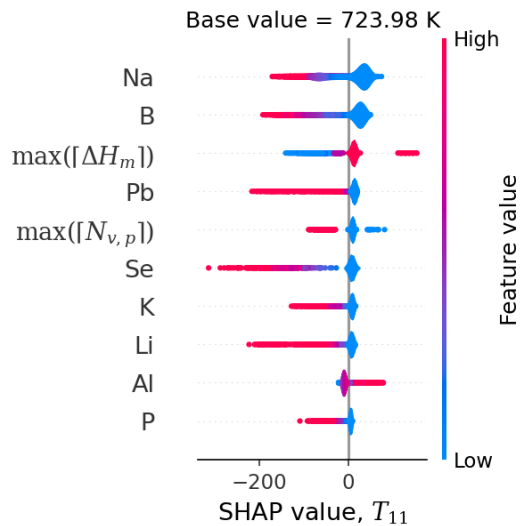


Figure S.12: Violin plot of SHAP values for T_{11} .

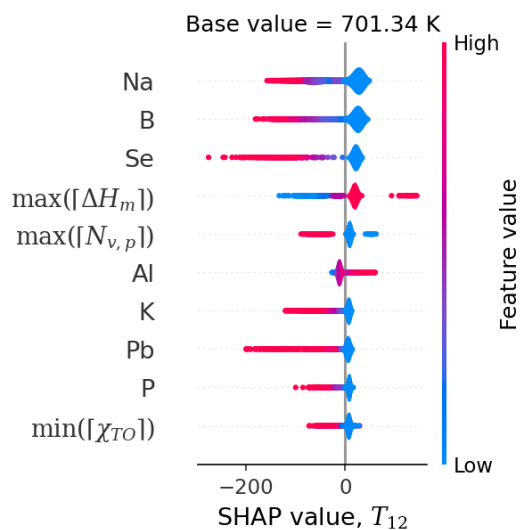


Figure S.13: Violin plot of SHAP values for T_{12} .

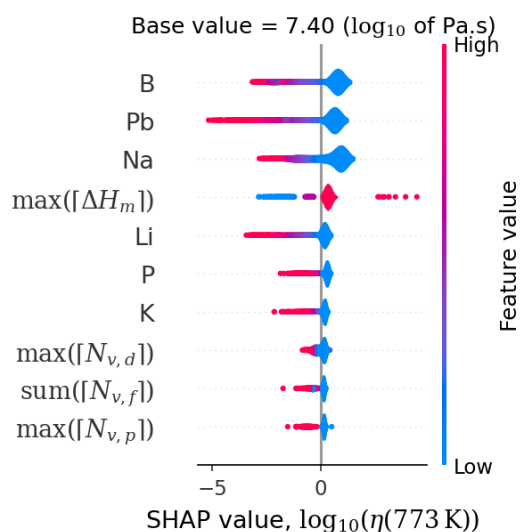


Figure S.14: Violin plot of SHAP values for $\log_{10}(\eta(773 \text{ K}))$.

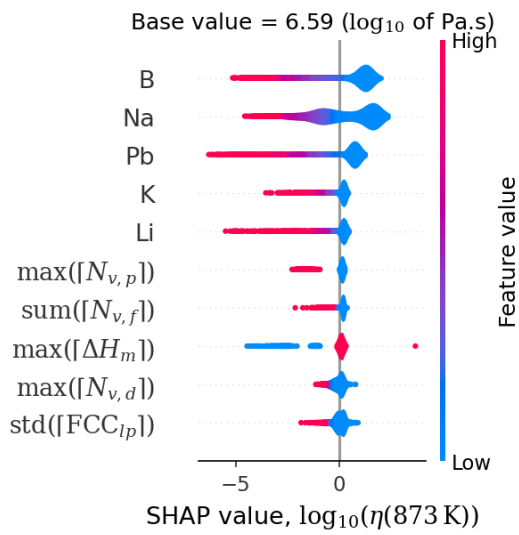


Figure S.15: Violin plot of SHAP values for log₁₀(η(873 K)).

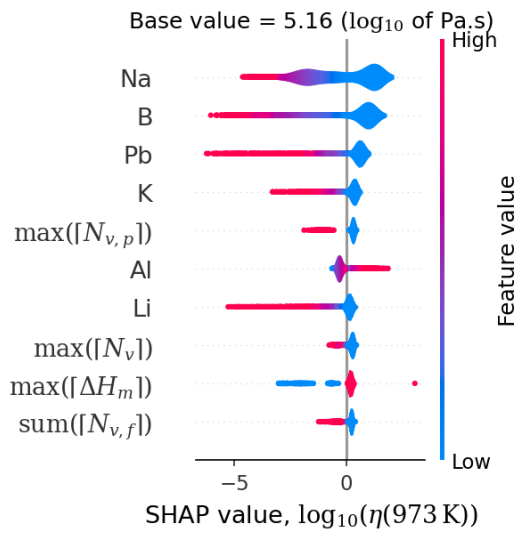


Figure S.16: Violin plot of SHAP values for log₁₀(η(973 K)).

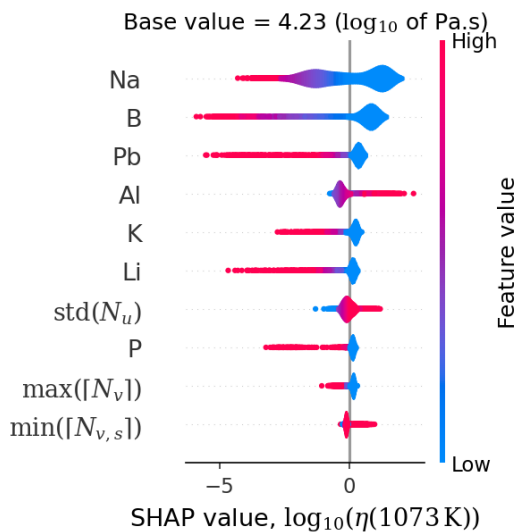


Figure S.17: Violin plot of SHAP values for log₁₀(η(1073 K)).

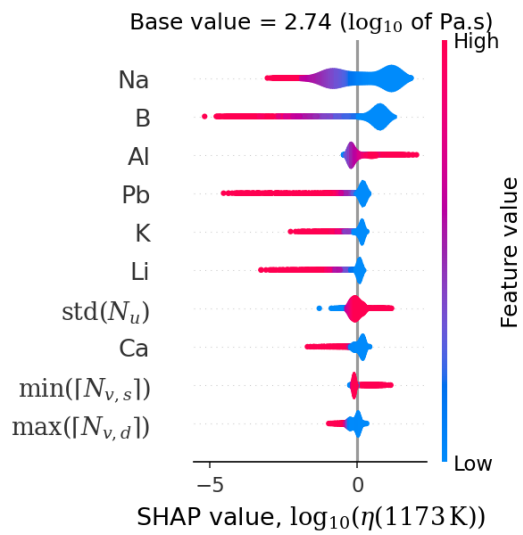


Figure S.18: Violin plot of SHAP values for $\log_{10}(\eta(1173\text{K}))$.

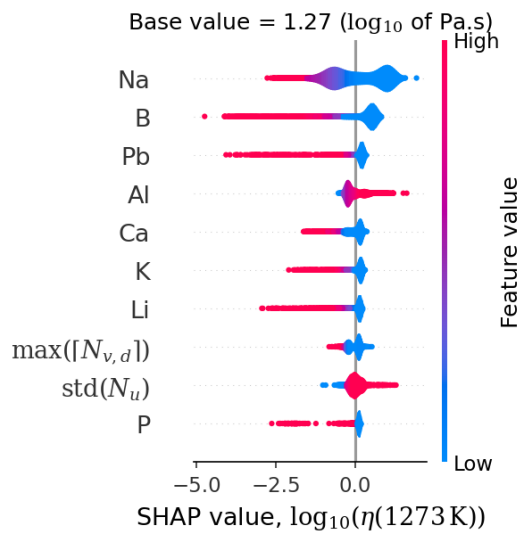


Figure S.19: Violin plot of SHAP values for $\log_{10}(\eta(1273\text{K}))$.

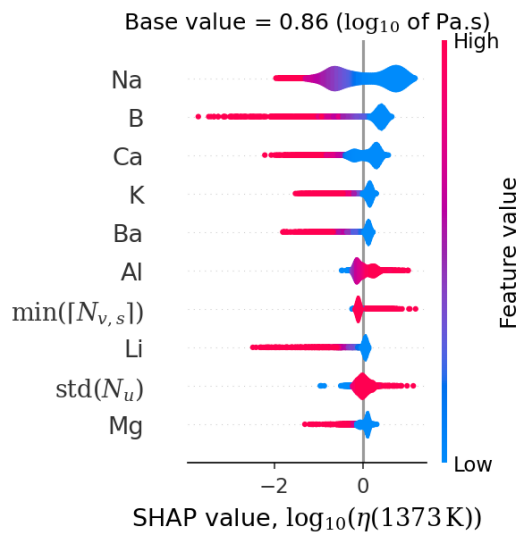


Figure S.20: Violin plot of SHAP values for $\log_{10}(\eta(1373\text{K}))$.

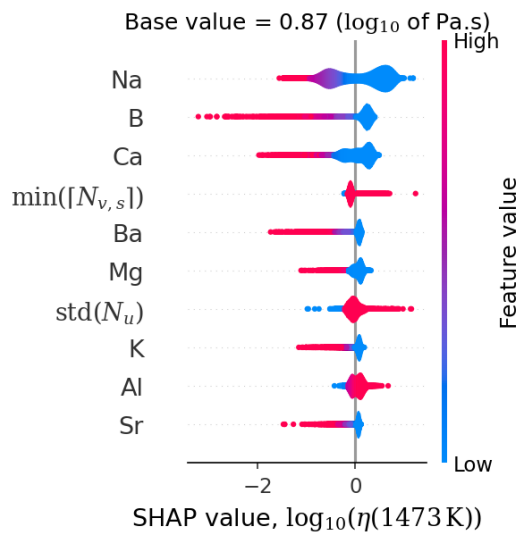


Figure S.21: Violin plot of SHAP values for log₁₀(η(1473 K)).

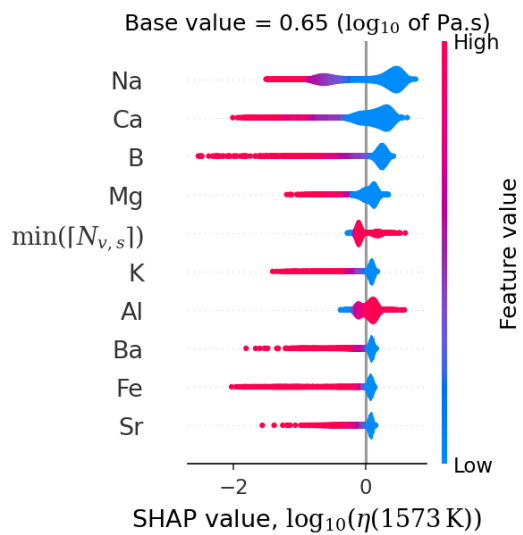


Figure S.22: Violin plot of SHAP values for log₁₀(η(1573 K)).

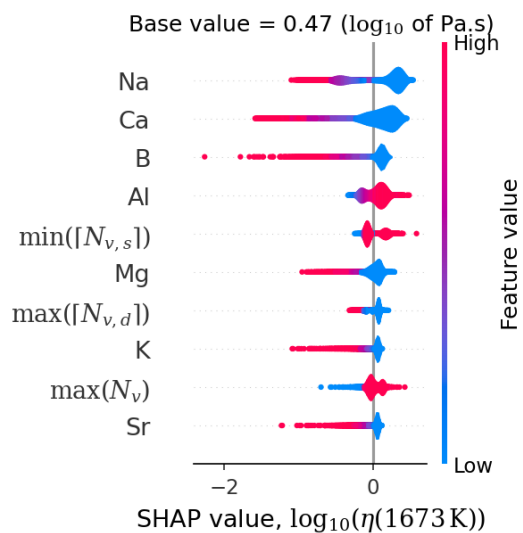


Figure S.23: Violin plot of SHAP values for log₁₀(η(1673 K)).

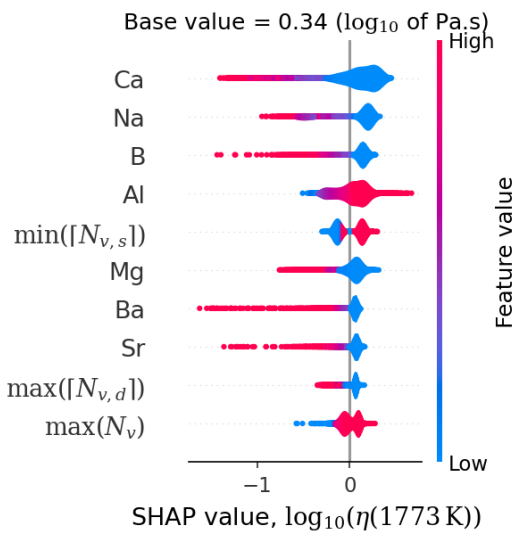


Figure S.24: Violin plot of SHAP values for $\log_{10}(\eta(1773\text{ K}))$.

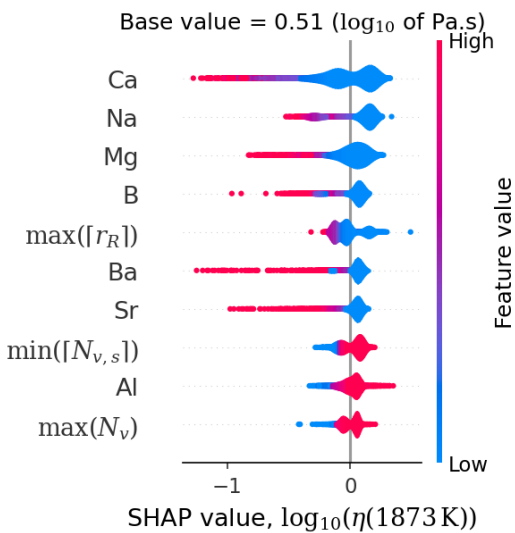


Figure S.25: Violin plot of SHAP values for $\log_{10}(\eta(1873\text{ K}))$.

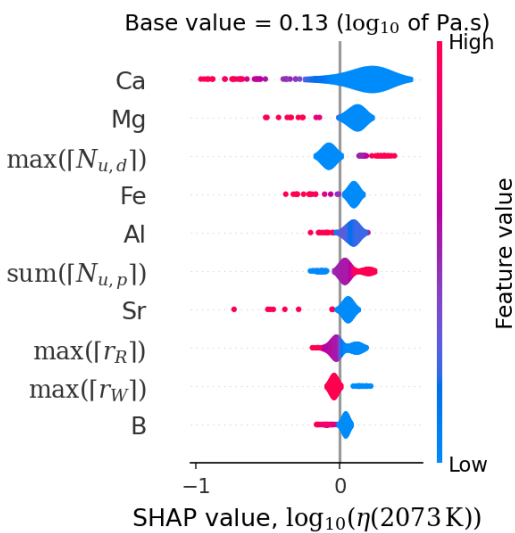


Figure S.26: Violin plot of SHAP values for $\log_{10}(\eta(2073\text{ K}))$.

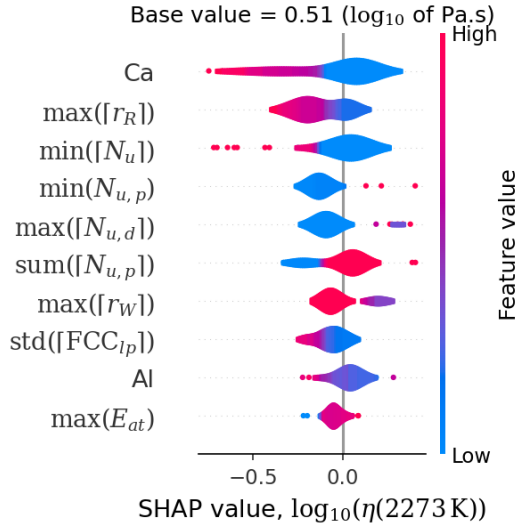


Figure S.27: Violin plot of SHAP values for log₁₀(η (2273 K)).

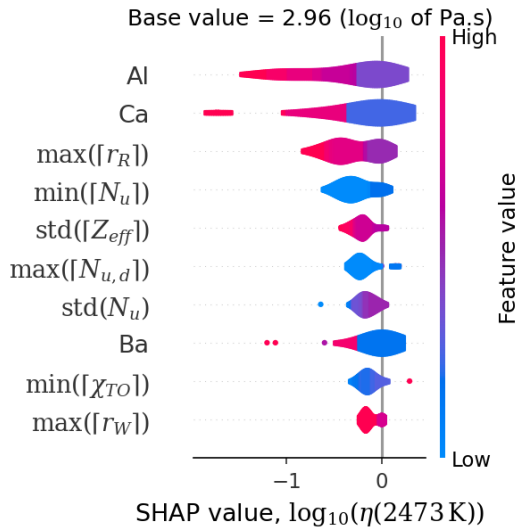


Figure S.28: Violin plot of SHAP values for log₁₀(η (2473 K)). This is the only violin plot in this set computed using the MLP model instead of the multi-headed model.

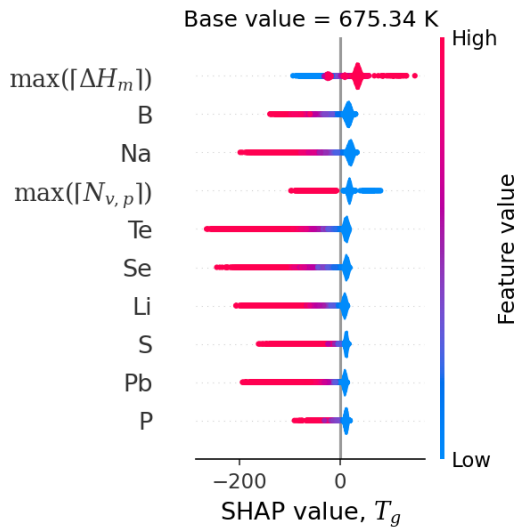


Figure S.29: Violin plot of SHAP values for T_g.

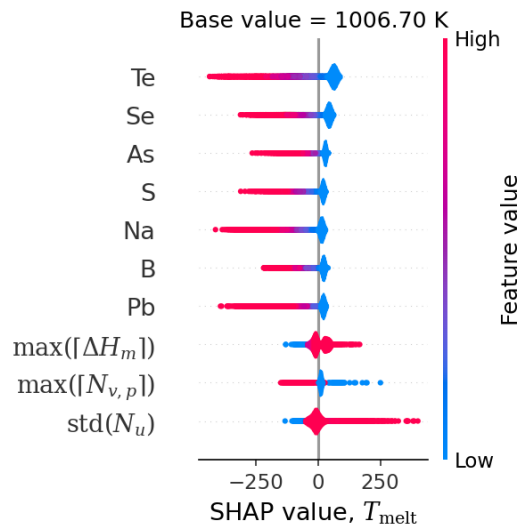


Figure S.30: Violin plot of SHAP values for T_{melt} .

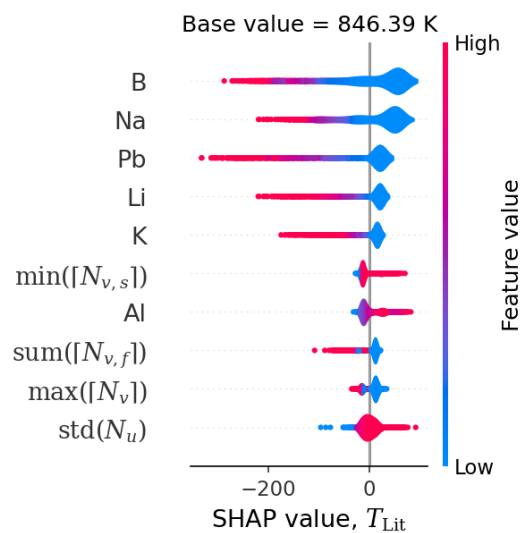


Figure S.31: Violin plot of SHAP values for T_{Lit} .

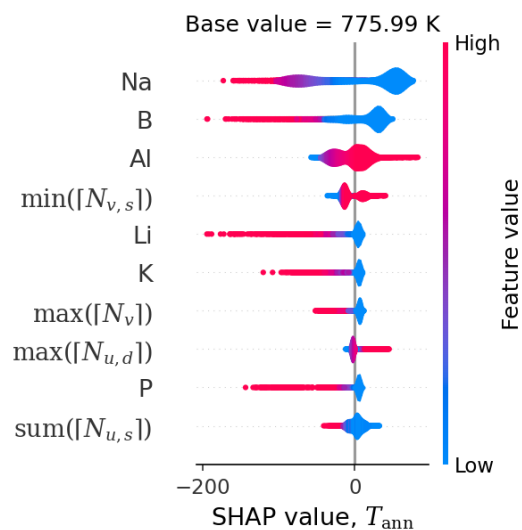


Figure S.32: Violin plot of SHAP values for T_{ann} .

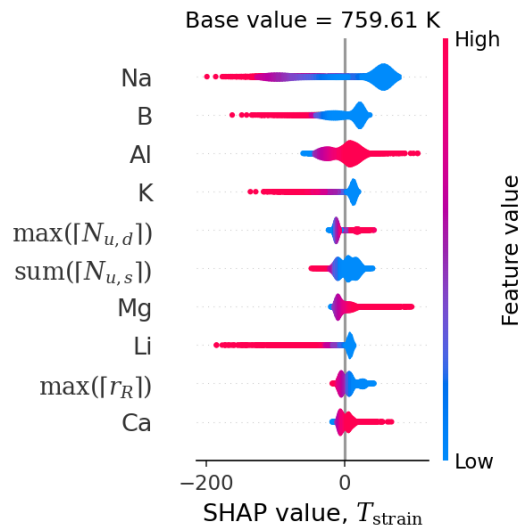


Figure S.33: Violin plot of SHAP values for T_{strain} .

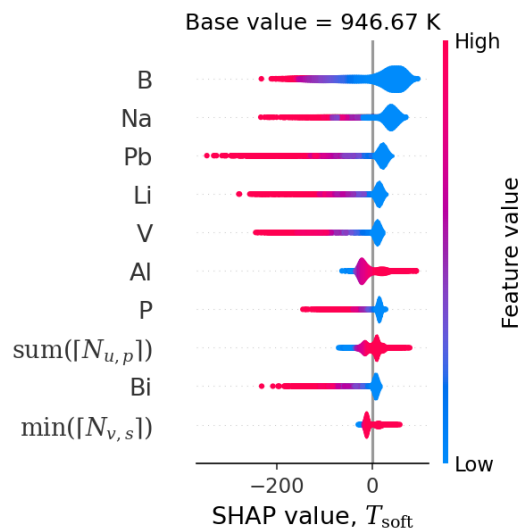


Figure S.34: Violin plot of SHAP values for T_{soft} .

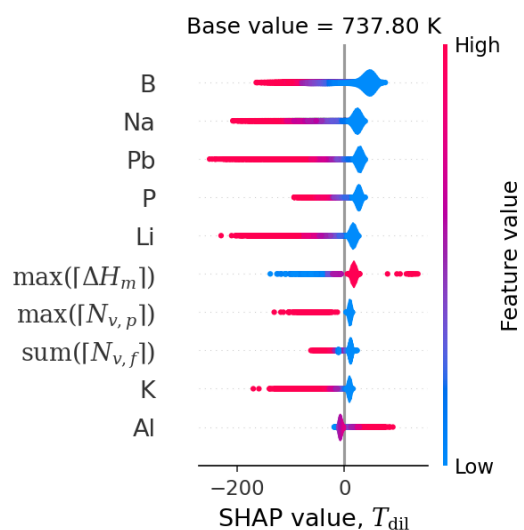


Figure S.35: Violin plot of SHAP values for T_{dil} .

SHAP values violin plots — optical properties

Figures S.36 to S.40 show the violin plots of the SHAP values for the optical properties. The SHAP values were calculated using the multi-headed GlassNet model.

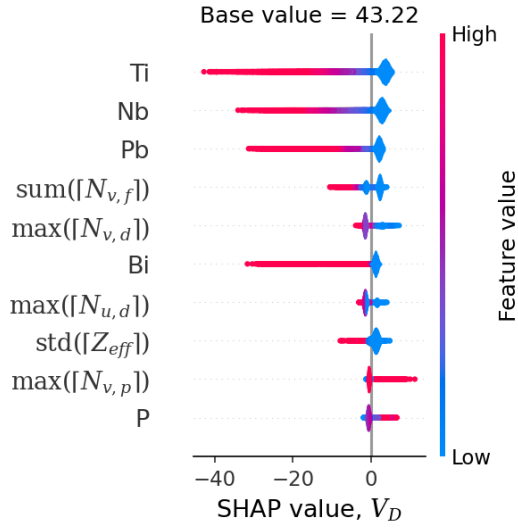


Figure S.36: Violin plot of SHAP values for V_D .

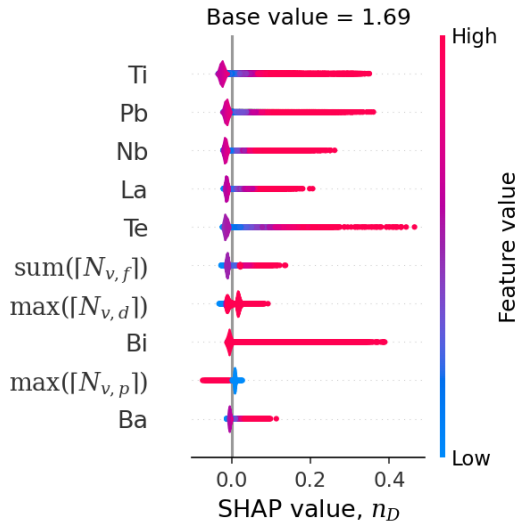


Figure S.37: Violin plot of SHAP values for n_D .

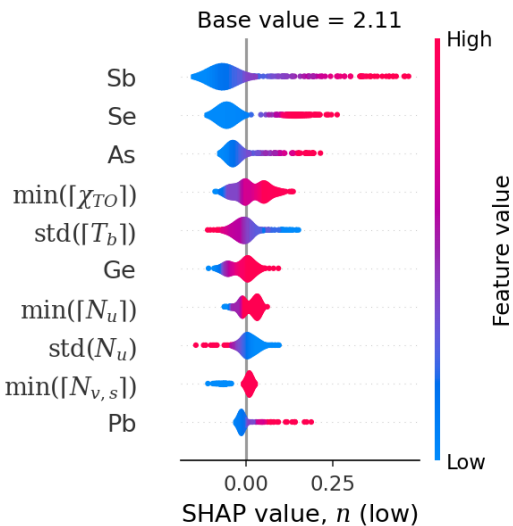


Figure S.38: Violin plot of SHAP values for n (low).

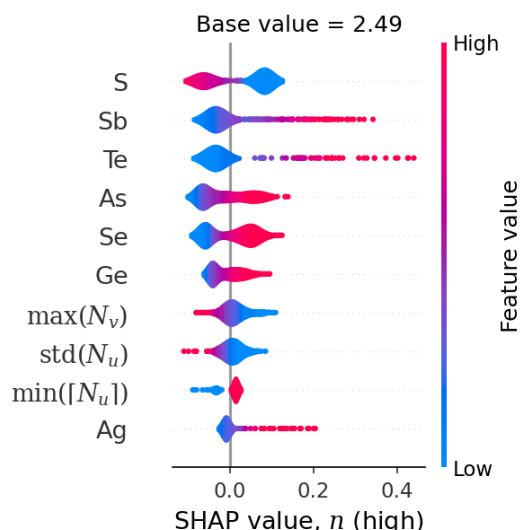


Figure S.39: Violin plot of SHAP values for n (high).

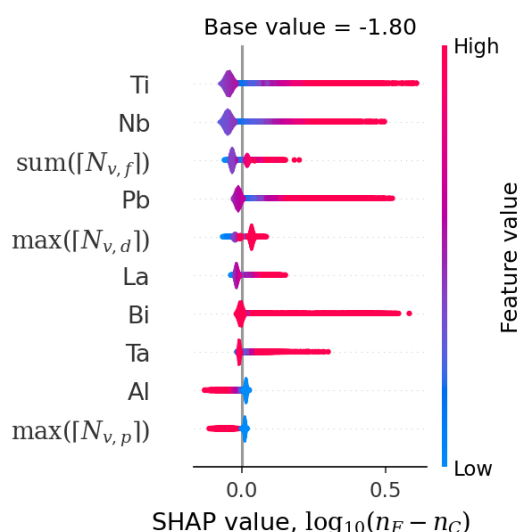


Figure S.40: Violin plot of SHAP values for $\log_{10}(n_F - n_C)$.

SHAP values violin plots — electrical and dielectric properties

Figures S.41 to S.51 show the violin plots of the SHAP values for the electrical and dielectric properties. The SHAP values were calculated using the multi-headed GlassNet model.

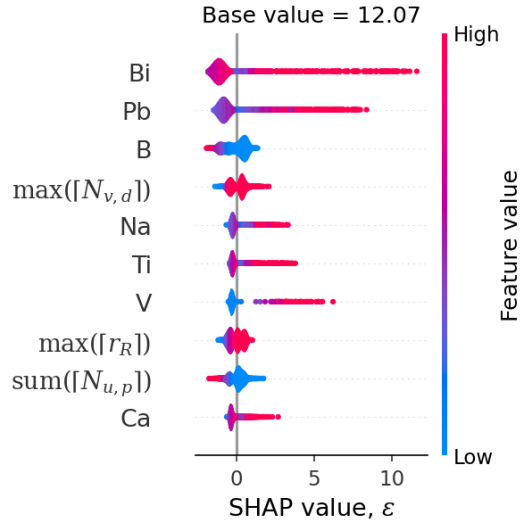


Figure S.41: Violin plot of SHAP values for ϵ .

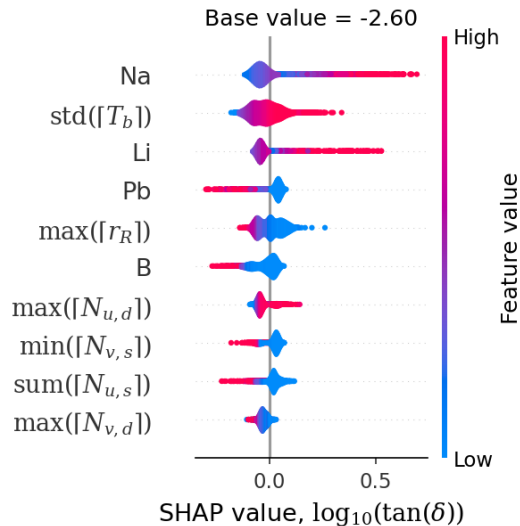


Figure S.42: Violin plot of SHAP values for $\log_{10}(\tan(\delta))$.

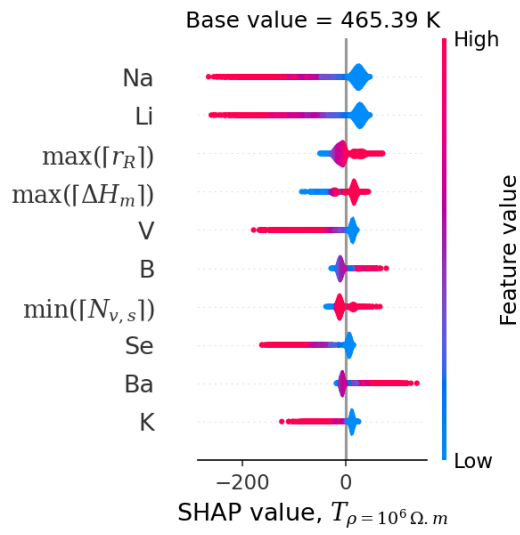


Figure S.43: Violin plot of SHAP values for $T_{\rho}=10^6 \Omega.m$.

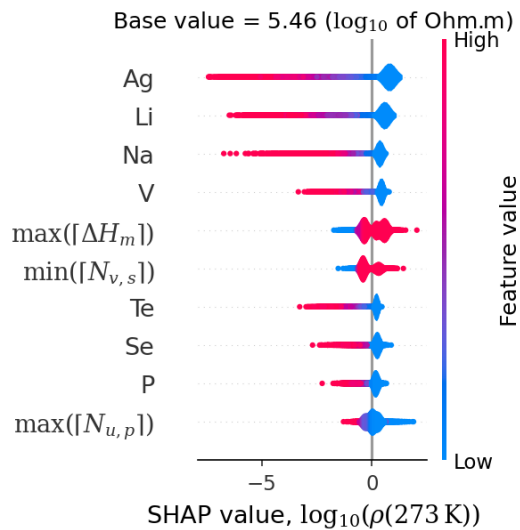


Figure S.44: Violin plot of SHAP values for $\log_{10}(\rho(273 K))$.

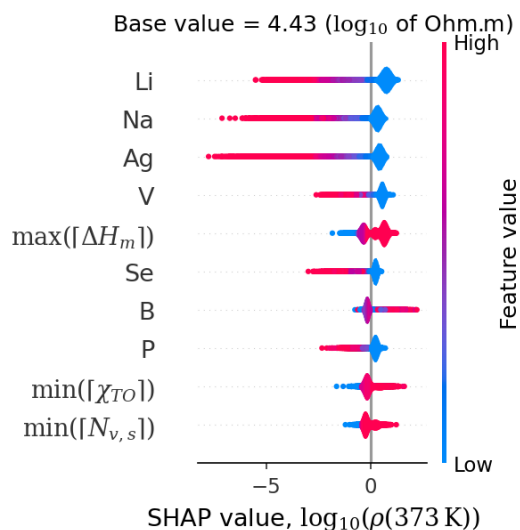


Figure S.45: Violin plot of SHAP values for $\log_{10}(\rho(373 K))$.

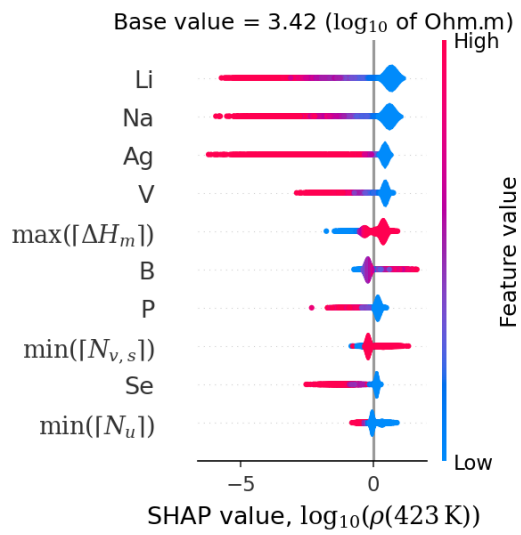


Figure S.46: Violin plot of SHAP values for $\log_{10}(\rho(423 \text{ K}))$.

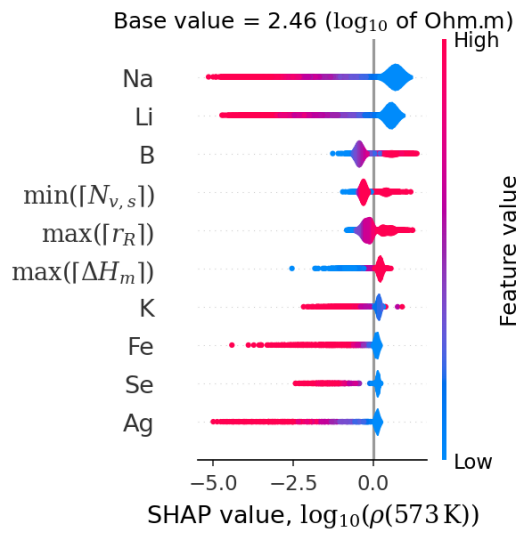


Figure S.47: Violin plot of SHAP values for $\log_{10}(\rho(573 \text{ K}))$.

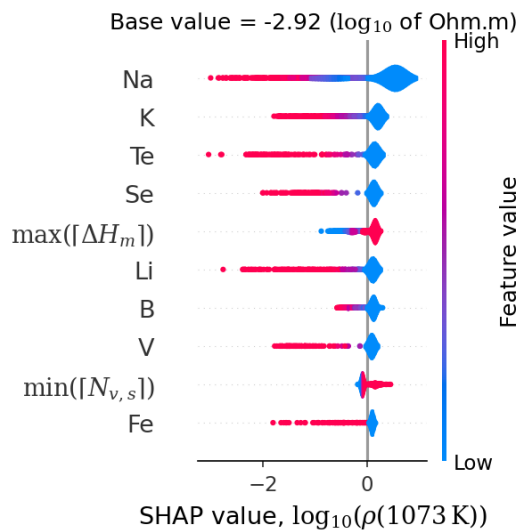


Figure S.48: Violin plot of SHAP values for $\log_{10}(\rho(1073 \text{ K}))$.

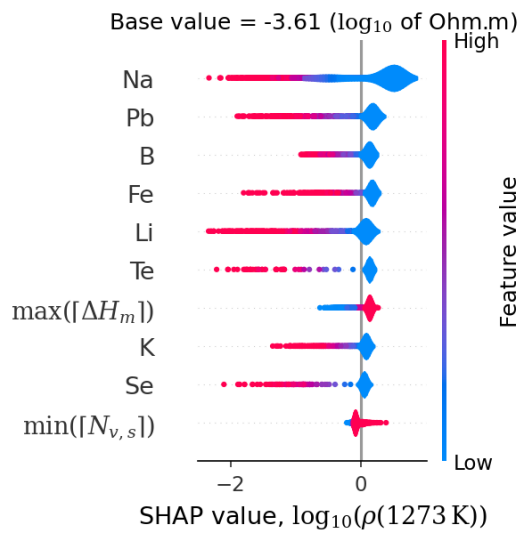


Figure S.49: Violin plot of SHAP values for $\log_{10}(\rho(1273 \text{ K}))$.

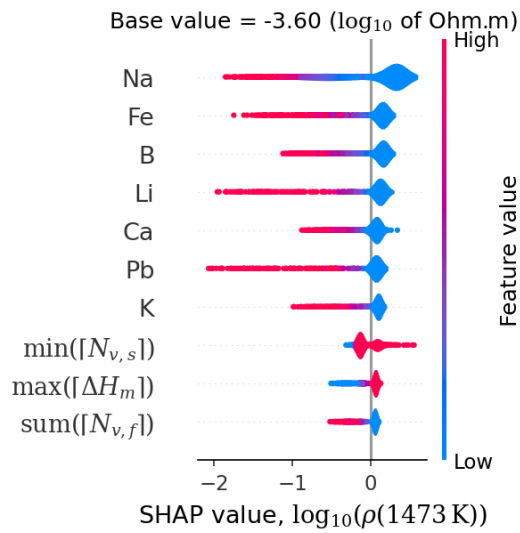


Figure S.50: Violin plot of SHAP values for $\log_{10}(\rho(1473 \text{ K}))$.

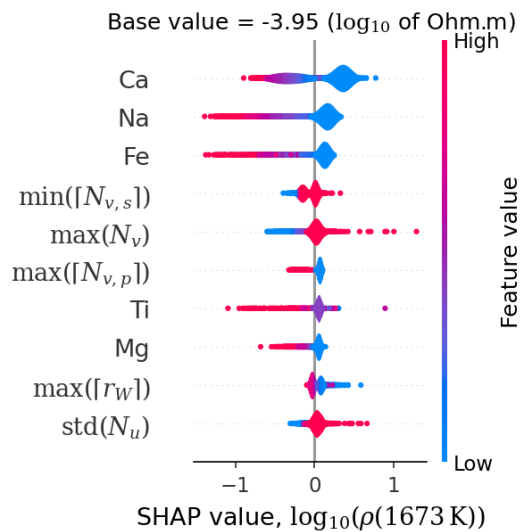


Figure S.51: Violin plot of SHAP values for $\log_{10}(\rho(1673 \text{ K}))$.

SHAP values violin plots — mechanical properties

Figures S.52 to S.55 show the violin plots of the SHAP values for the mechanical properties. The SHAP values were calculated using the multi-headed GlassNet model.

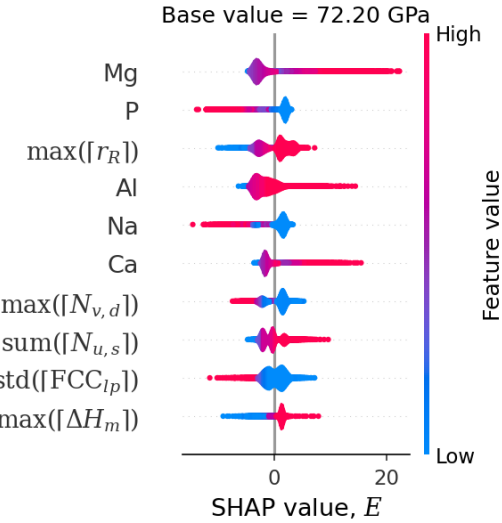


Figure S.52: Violin plot of SHAP values for E .

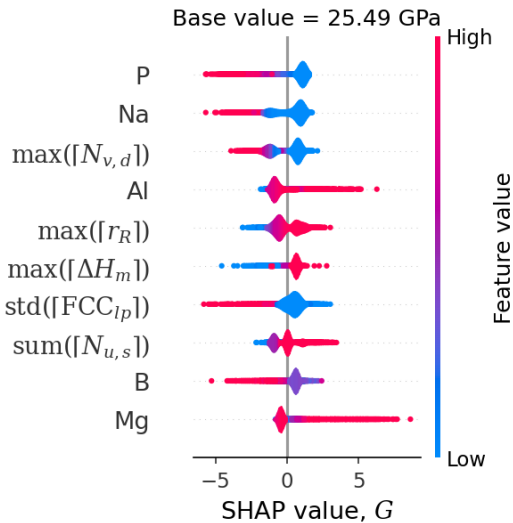


Figure S.53: Violin plot of SHAP values for G .

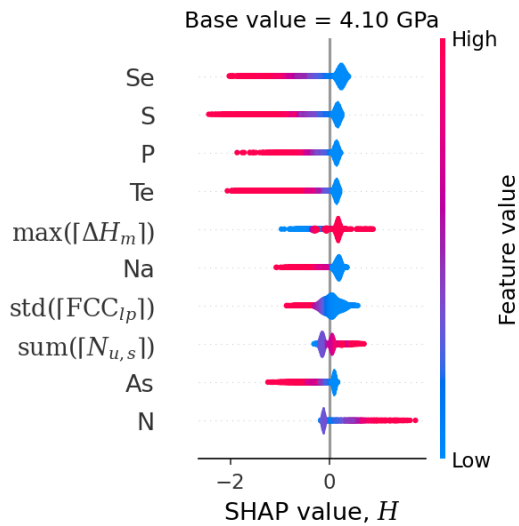


Figure S.54: Violin plot of SHAP values for H .

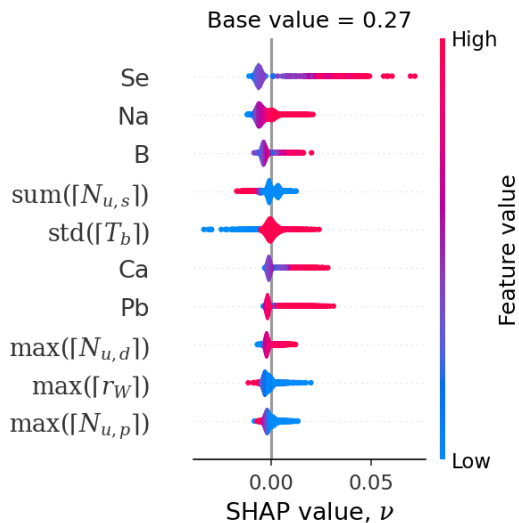


Figure S.55: Violin plot of SHAP values for ν .

SHAP values violin plots — density

Figures S.56 to S.60 show the violin plots of the SHAP values for the glass density at different temperatures. The SHAP values were calculated using the multi-headed GlassNet model.

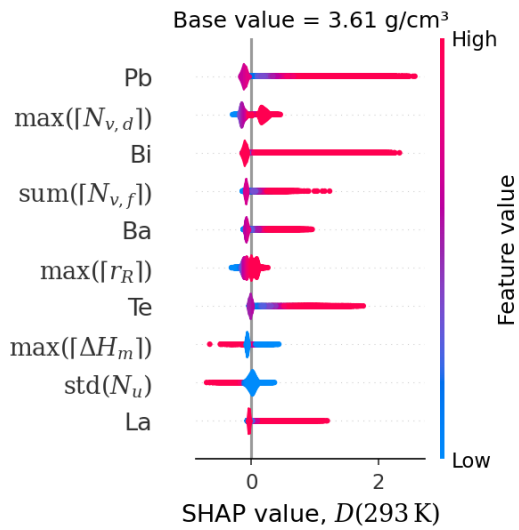


Figure S.56: Violin plot of SHAP values for $D(293\text{ K})$.

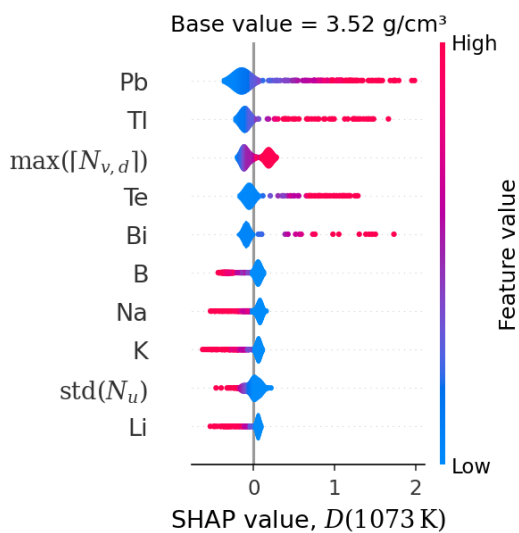


Figure S.57: Violin plot of SHAP values for $D(1073\text{ K})$.

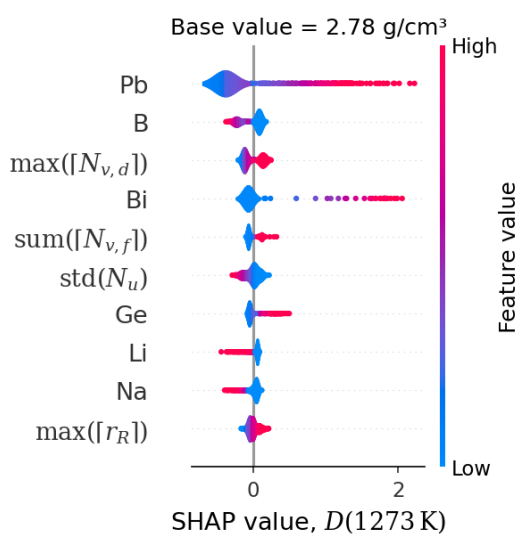


Figure S.58: Violin plot of SHAP values for $D(1273\text{ K})$.

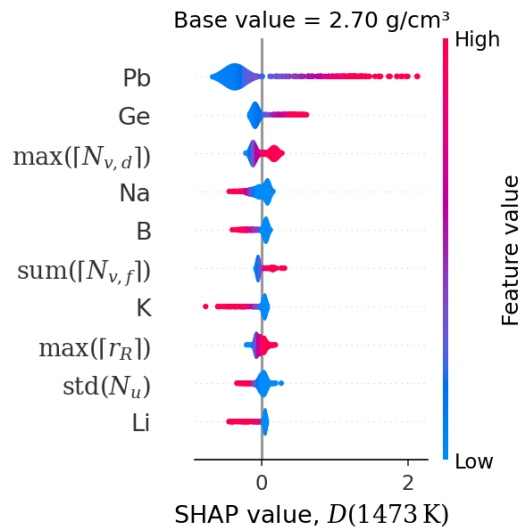


Figure S.59: Violin plot of SHAP values for $D(1473\text{ K})$.

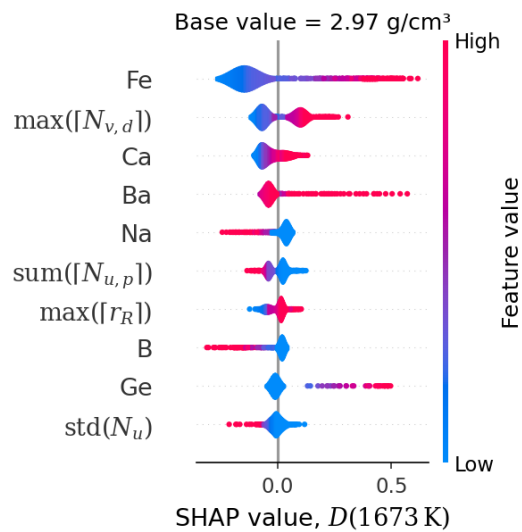


Figure S.60: Violin plot of SHAP values for $D(1673\text{ K})$.

SHAP values violin plots — thermal properties

Figures S.61 to S.74 show the violin plots of the SHAP values for the thermal properties. The SHAP values were calculated using the multi-headed GlassNet model.

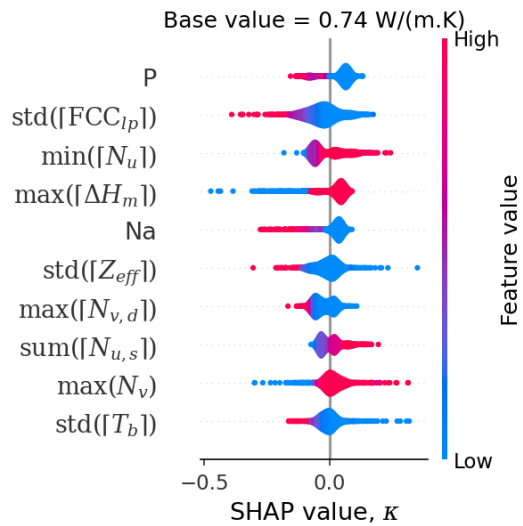


Figure S.61: Violin plot of SHAP values for κ .

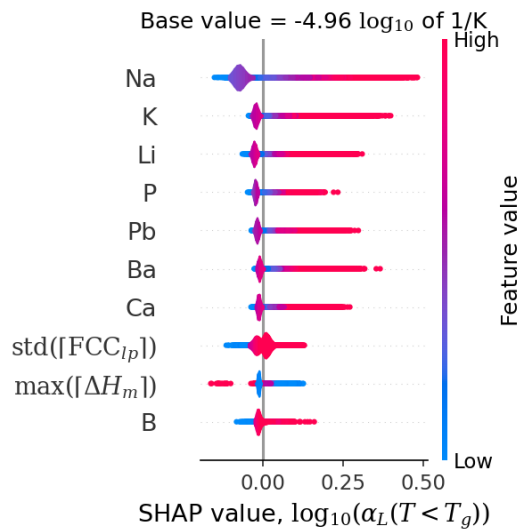


Figure S.62: Violin plot of SHAP values for log₁₀($\alpha_L(T < T_g)$).

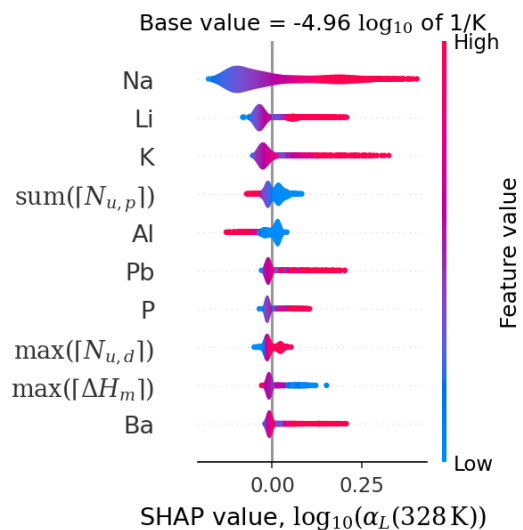


Figure S.63: Violin plot of SHAP values for log₁₀($\alpha_L(328\text{ K})$).

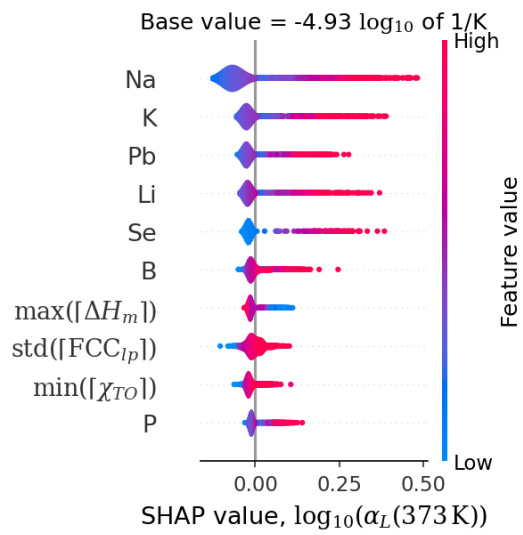


Figure S.64: Violin plot of SHAP values for $\log_{10}(\alpha_L(373\text{ K}))$.

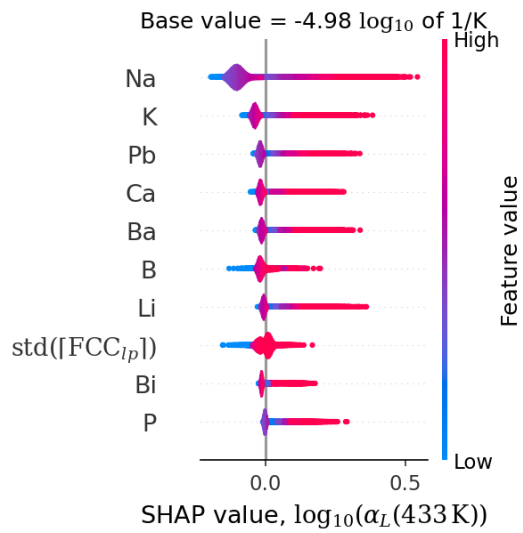


Figure S.65: Violin plot of SHAP values for $\log_{10}(\alpha_L(433\text{ K}))$.

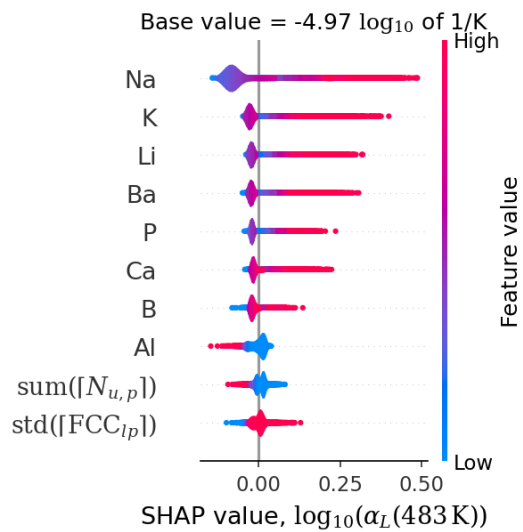


Figure S.66: Violin plot of SHAP values for $\log_{10}(\alpha_L(483\text{ K}))$.

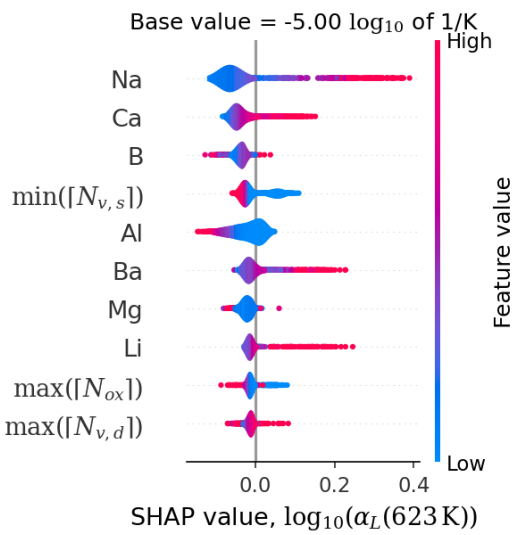


Figure S.67: Violin plot of SHAP values for $\log_{10}(\alpha_L(623\text{ K}))$.

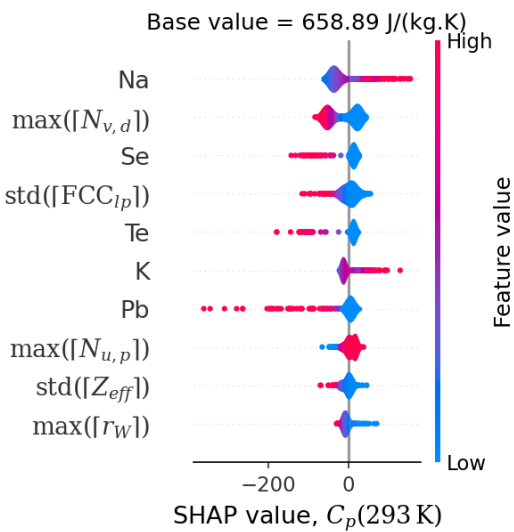


Figure S.68: Violin plot of SHAP values for $C_p(293\text{ K})$.

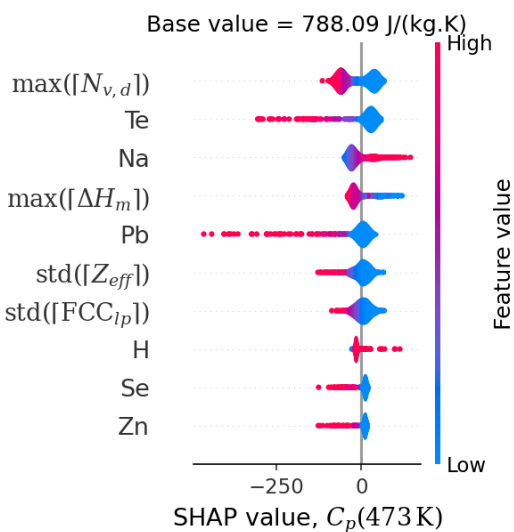


Figure S.69: Violin plot of SHAP values for $C_p(473\text{ K})$.

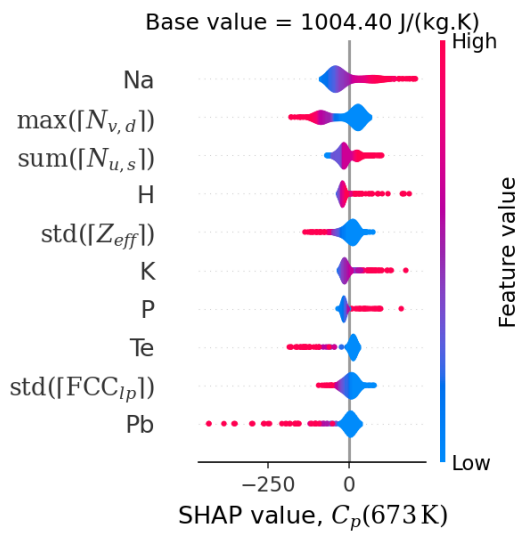


Figure S.70: Violin plot of SHAP values for $C_p(673\text{ K})$.

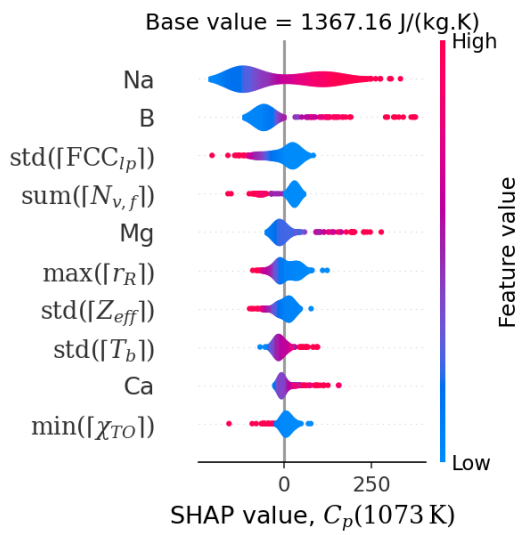


Figure S.71: Violin plot of SHAP values for $C_p(1073\text{ K})$.

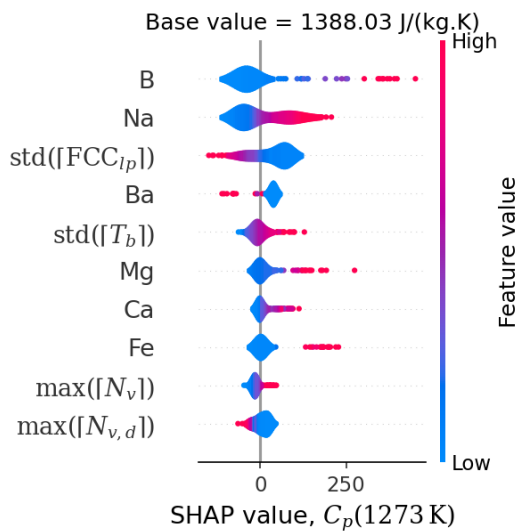


Figure S.72: Violin plot of SHAP values for $C_p(1273\text{ K})$.

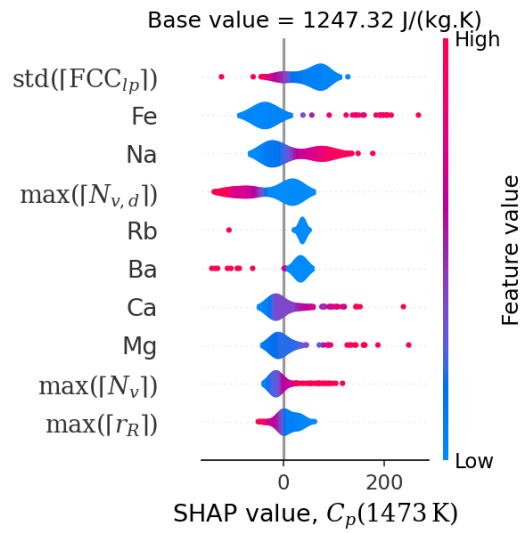


Figure S.73: Violin plot of SHAP values for $C_p(1473 \text{ K})$.

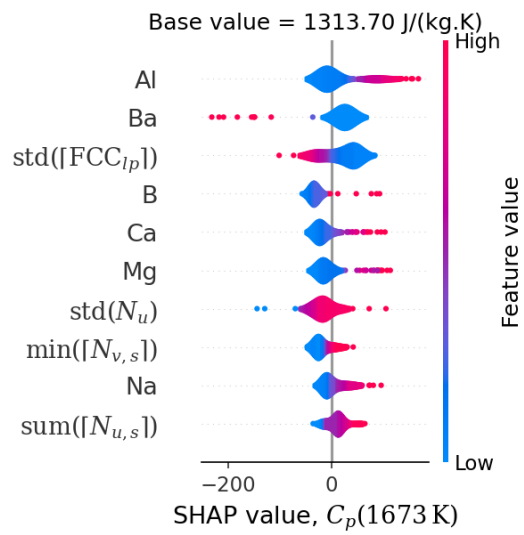


Figure S.74: Violin plot of SHAP values for $C_p(1673 \text{ K})$.

SHAP values violin plots — crystallization

Figures S.75 to S.78 show the violin plots of the SHAP values for properties related to crystallization. The SHAP values were calculated using the multi-headed GlassNet model.

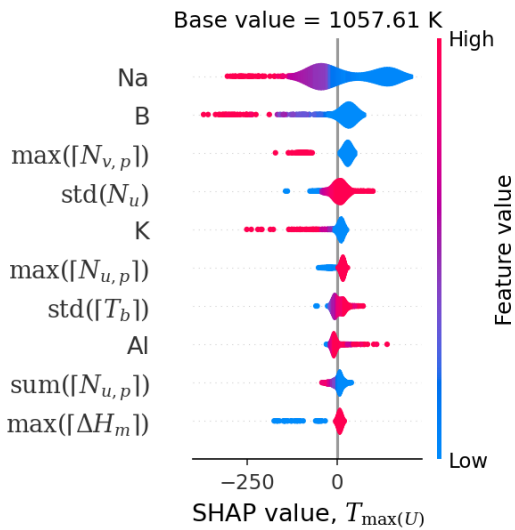


Figure S.75: Violin plot of SHAP values for $T_{\max(U)}$.

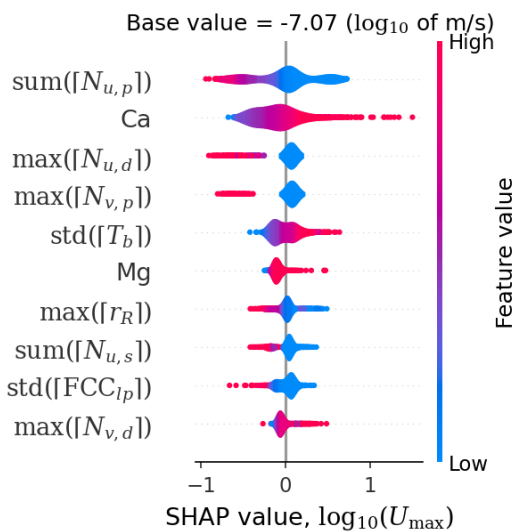


Figure S.76: Violin plot of SHAP values for $\log_{10}(U_{\max})$.

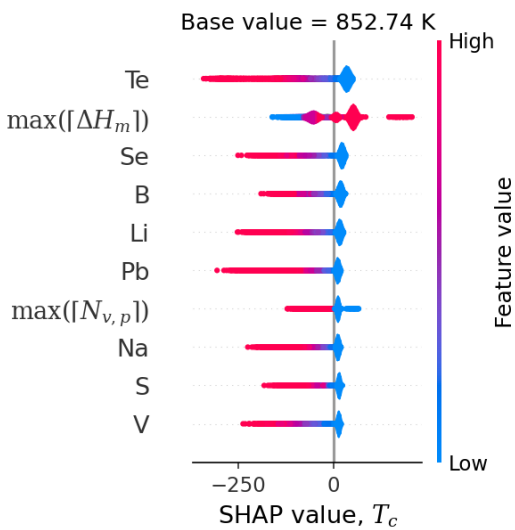


Figure S.77: Violin plot of SHAP values for T_c .

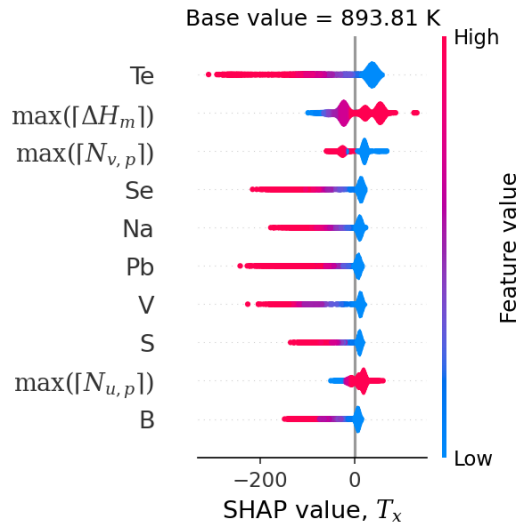


Figure S.78: Violin plot of SHAP values for T_x .

SHAP values violin plots — surface tension

Figures S.79 to S.83 show the violin plots of the SHAP values for the surface tension at different temperatures. The SHAP values were calculated using the multi-headed GlassNet model.

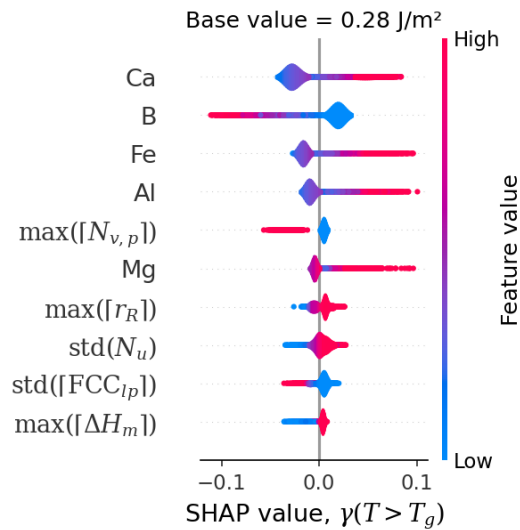


Figure S.79: Violin plot of SHAP values for $\gamma(T > T_g)$.

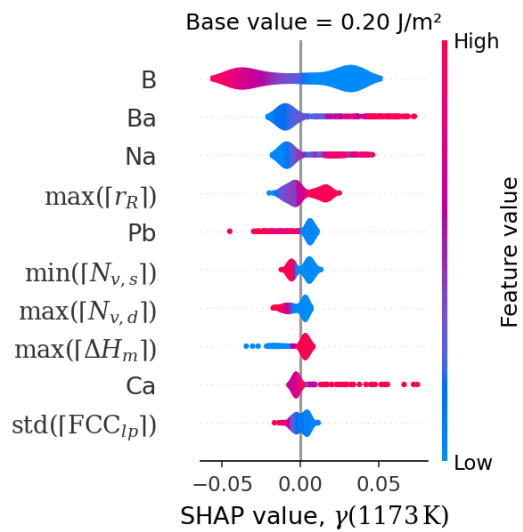


Figure S.80: Violin plot of SHAP values for $\gamma(1173\text{ K})$.

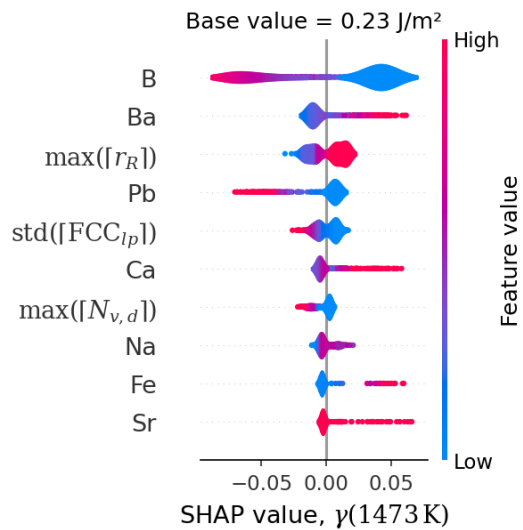


Figure S.81: Violin plot of SHAP values for $\gamma(1473\text{ K})$.

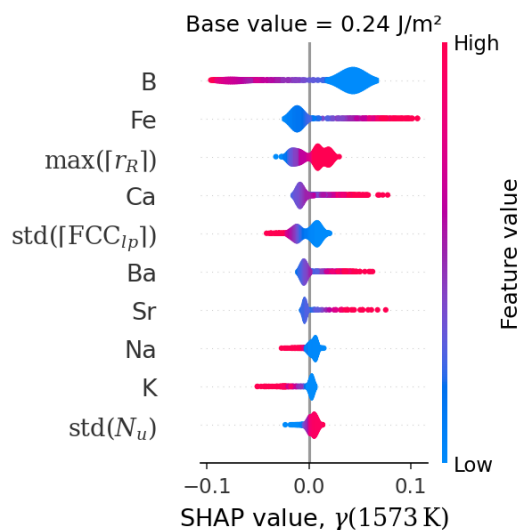


Figure S.82: Violin plot of SHAP values for $\gamma(1573\text{ K})$.

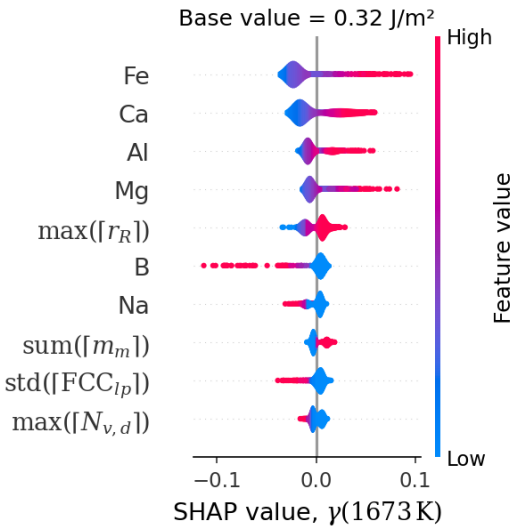


Figure S.83: Violin plot of SHAP values for $\gamma(1673 \text{ K})$.

SHAP values violin plots — liquidus temperature and thermal shock resistance

Figures S.84 and S.85 show the violin plots of the SHAP values for the liquidus temperature and the thermal shock resistance, respectively. The SHAP values were calculated using the multi-headed GlassNet model.

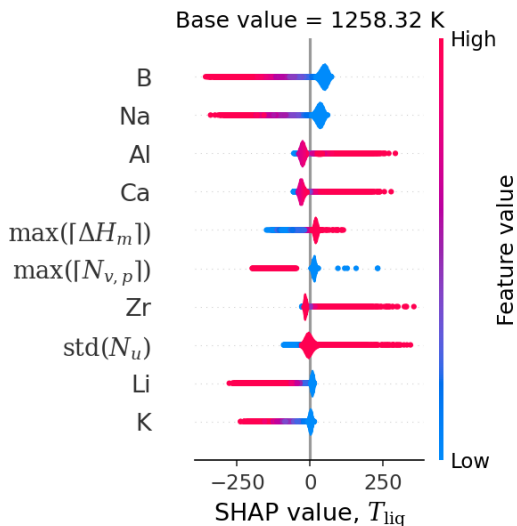


Figure S.84: Violin plot of SHAP values for T_{liq} .

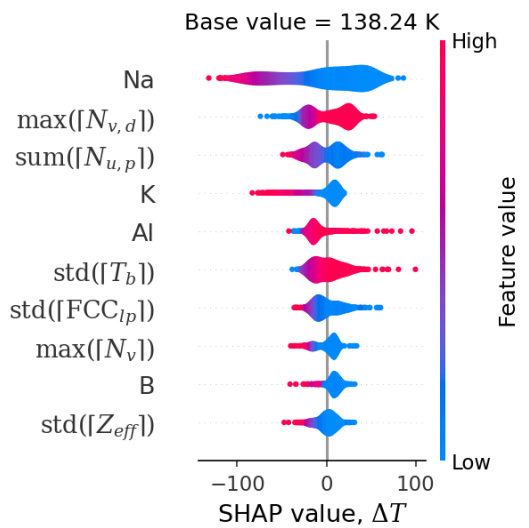


Figure S.85: Violin plot of SHAP values for ΔT .